

# Denudation and Weathering Rates of Carbonate Landscapes From Meteoric $^{10}\text{Be}/^9\text{Be}$ Ratios



### Key Points:

- Denudation rates from  $^{10}\text{Be}/^9\text{Be}$  in a carbonate landscape agree within a factor of 2 with rates from suspended and dissolved river loads
- Meteoric  $^{10}\text{Be}/^9\text{Be}$ -derived carbonate denudation is dominated by weathering ( $>0.9$  W/D)
- A non-negligible contribution in denudation originates in deeper (below soil) weathering

### Correspondence to:

H. Wittmann,  
hella.wittmann-oele@gfz-potsdam.de

### Citation:






Wittmann, H., Bouchez, J., Calmels, D., Gaillardet, J., Frick, D. A., Stroncik, N., et al. (2024). Denudation and weathering rates of carbonate landscapes from meteoric  $^{10}\text{Be}/^9\text{Be}$  ratios. *Journal of Geophysical Research: Earth Surface*, 129, e2024JF007638. <https://doi.org/10.1029/2024JF007638>

Received 10 JAN 2024

Accepted 22 JUL 2024

### Author Contributions:

**Conceptualization:** H. Wittmann, J. Bouchez, J. Gaillardet, F. von Blanckenburg  
**Data curation:** H. Wittmann  
**Funding acquisition:** J. Gaillardet  
**Investigation:** H. Wittmann, J. Bouchez, F. von Blanckenburg  
**Methodology:** H. Wittmann, J. Bouchez, D. A. Frick, N. Stroncik  
**Project administration:** H. Wittmann  
**Resources:** J. Bouchez, J. Gaillardet, D. A. Frick, ASTER Team  
**Validation:** H. Wittmann  
**Visualization:** H. Wittmann  
**Writing – original draft:** H. Wittmann, J. Bouchez, F. von Blanckenburg

H. Wittmann<sup>1</sup> , J. Bouchez<sup>2</sup> , D. Calmels<sup>3</sup>, J. Gaillardet<sup>2</sup> , D. A. Frick<sup>1,4</sup> , N. Stroncik<sup>1</sup> , ASTER Team<sup>5</sup>, and F. von Blanckenburg<sup>6</sup>

<sup>1</sup>GFZ German Research Centre for Geosciences, Potsdam, Germany, <sup>2</sup>Institut de physique du globe de Paris, CNRS, Université de Paris, Paris, France, <sup>3</sup>Laboratoire GEOPS, CNRS, Université Paris-Saclay, Orsay, France, <sup>4</sup>Now at Institute of Geosciences, Kiel University, Kiel, Germany, <sup>5</sup>Aix-Marseille University, CNRS, IRD, INRA, Coll France, CEREGE, Technopôle de l'Environnement Arbois-Méditerranée, Aix-en-Provence, France, <sup>6</sup>Institute of Geological Sciences, Freie Universität Berlin, Berlin, Germany

**Abstract** Knowledge of the rates of carbonate rock denudation, the relative apportionment of chemical weathering versus physical erosion, and their sensitivity to climate, vegetation, and tectonics is essential for disclosing feedbacks within the carbon cycle and the functioning of karst landscapes that supply important services to humans. Currently, however, for carbonate lithologies, no method exists that allows to simultaneously partition denudation into erosion and weathering fluxes at spatial scales ranging from soil to watersheds. To determine total denudation rates in carbonate landscapes from an individual soil or river sample, we adapted a published framework that combines cosmogenic meteoric  $^{10}\text{Be}$  as an atmospheric flux tracer with stable  $^9\text{Be}$  that is released from rocks by weathering, to the limestone-dominated French Jura Mountains. By analyzing water, soil, sediment, travertine, and bedrock for  $^{10}\text{Be}/^9\text{Be}$ , major and trace elements, carbon stable isotopes and radiogenic strontium, we quantified contributions of Be from primary versus secondary carbonate phases and its release during weathering from carbonate bedrock versus silicate impurities. We calculated partitioning of Be between solids and solutes, and rates of catchment-wide (from sediment) and point source (from soil) denudation, weathering and erosion. Our results indicate that average denudation rates are 300–500 t/km<sup>2</sup>/yr. Denudation is dominated by weathering intensity (W/D) ratios of  $>0.92$ , and a non-negligible contribution from deeper (below soil) weathering. Our rates agree to within less than a factor of two with decadal-scale denudation rates from combined suspended and dissolved fluxes, highlighting the substantial potential of this method for future Earth surface studies.

**Plain Language Summary** Carbonate rocks, constituting about 10% of the terrestrial Earth's surface, play a crucial role in the short-term carbon cycle by absorbing atmospheric CO<sub>2</sub> and forming karst landscapes. These landscapes, supporting 10% of the global population with vital services, remain poorly understood due to a lack of tools for assessing erosion and weathering rates. In our study of the French Jura Mountains, we utilized a novel method involving the isotope ratio of  $^{10}\text{Be}/^9\text{Be}$  from the cosmogenic meteoric  $^{10}\text{Be}$ , raining onto Earth from the atmosphere at a specific rate, and the stable trace element  $^9\text{Be}$  released from rocks by weathering, to measure erosion, weathering, and total denudation. Our results indicate an annual soil and sediment erosion of 300–500 tons per square kilometer, with 90% attributed to rock dissolution (weathering) and 10% to physical erosion. A non-trivial fraction of weathering appears to happen deep (below soil). Our new rates agree closely with rates estimated independently from suspended and dissolved river loads. As such, they demonstrate the considerable potential of the  $^{10}\text{Be}/^9\text{Be}$  technique as a rate meter at Earth's surface.

## 1. Introduction

Carbonate rocks comprise about 10% of the land surface (J. Hartmann & Moosdorf, 2012), providing home to 1.2 billion people in 2015, and about 9% of the world's population is supplied by karst waters (Goldscheider et al., 2020). Yet karst environments are extremely fragile. Karst waters are undergoing rapid change in chemistry due to environmental change (Jeannin et al., 2016), and at many locations intense land use has led to a transformation of once soil-covered karst into barren landscapes that cannot provide food security. Re-establishment of a soil layer and hence vegetation cover is however exceedingly slow in carbonate rocks because they contain little insoluble material (Xiao & Weng, 2007). Globally, carbonate rocks are also important players in the carbon cycle. Weathering of carbonate rocks induces an uptake of atmospheric CO<sub>2</sub> similar to that derived from silicate

© 2024. The Author(s).

This is an open access article under the terms of the [Creative Commons Attribution License](https://creativecommons.org/licenses/by/4.0/), which permits use, distribution and reproduction in any medium, provided the original work is properly cited.

weathering, and exerts a profound impact on ocean carbonate chemistry as about 60% of the dissolved solids transported into the oceans originate from carbonate rocks (Gaillardet et al., 1999). Their weathering thus generates the largest land-to sea flux of Ca, Mg, and inorganic C. However, the carbonate-sourced CO<sub>2</sub> withdrawal does not present a CO<sub>2</sub> sink over the time scale of millions of years, because the weathering reaction of carbonate on land is exactly balanced by the precipitation reaction in the oceans (Gaillardet et al., 2018). Carbonate weathering may still compensate anthropogenic CO<sub>2</sub> emissions transiently over a few hundreds to thousands of years (hereafter called “centennial” to “millennial” timescales), before re-precipitation of carbonate in the oceans (e.g., Archer, 2005; Beaulieu et al., 2012). When coupled to sulfuric acid release by sulfide oxidation, carbonate weathering can also act as a source of atmospheric CO<sub>2</sub> (Bufe et al., 2022; Calmels et al., 2007; Nevers et al., 2021).

Despite this significance of carbonate rock weathering, field estimates of the rates at which carbonate rock weather are still scarce. In most studies, these rates were determined from stream water chemistry (Binet et al., 2020; Calmels et al., 2014; Gaillardet et al., 2018; Han & Liu, 2004; J. Hartmann & Moosdorf, 2011). Such data often require deconvolution of fluxes from non-carbonate sources (e.g., Bufe et al., 2021, 2024), and include both surficial and deep karst weathering (Bakalowicz, 2015; Gunn, 2013). Studies exploring the dependence of carbonate weathering on soil depth and environmental variables are very rare, and depend on estimates of time such as from chronosequences (Jacobson et al., 2002) or reactive transport models (Dong et al., 2019).

In felsic igneous and siliciclastic lithologies denudation rates averaging over millennial time scales of soil formation and erosion have commonly been determined by means of the in situ produced cosmogenic <sup>10</sup>Be (Lal, 1991) over a large range of climatic and tectonic zones (e.g., Bierman & Nichols, 2004; Granger & Schaller, 2014; von Blanckenburg, 2005) and at nearly all scales from soil plots to very large river basins. For carbonate rocks that typically do not contain the quartz grains required for these measurements, other isotope systems are needed.

In pure carbonate lithologies, cosmogenic <sup>36</sup>Cl in situ produced in calcite has emerged as the nuclide of choice. Although its applications are still rare when compared to in situ <sup>10</sup>Be in quartz and are focused on sparsely-vegetated, arid- to semi-arid Mediterranean regions, patterns emerge from a global compilation of bedrock samples (Yang et al., 2020): where mean annual precipitation rates (MAP) are lower than 700 mm/yr, denudation rates increase with increasing precipitation rate, while at MAP above 700 mm/yr, carbonate denudation rates are thought to be mainly controlled by the kinetics of carbonate mineral dissolution. Only three studies so far conducted work in regions where MAP exceeds 1,300 mm/yr (Avni et al., 2019; Matsushi et al., 2010; Thomas et al., 2018) where denudation rates appear to decrease with MAP. If this decrease is not due to a bias, introduced for example, by sampling more weathering-resistant rocks like marble, a negative feedback between precipitation and weathering rate may be in operation. One property regulating such feedback could be vegetation-controlled soil pCO<sub>2</sub> (Calmels et al., 2014). Weathering in carbonate landscapes might thus be subject to sensitive feedbacks with climate and vegetation. However, before potential forcings and responses can be deciphered, two challenges need to be overcome.

- (1) Total denudation rates need to be deconvolved into rates of weathering and erosion. Both in situ cosmogenic <sup>36</sup>Cl- and <sup>10</sup>Be in calcite and quartz, respectively, yield the total denudation rate, that is, the sum of weathering rate and erosion rate. In pure limestone landscapes however, weathering dominates over erosion due to the high solubility of the constituents of carbonate rock: calcite and dolomite (Stallard & Edmond, 1987). The contribution of the weathering to denudation must therefore be determined by other means. These involve chemical depletion fractions (CDF), determined from the abundance of insoluble minerals in soil profiles (Ben-Asher et al., 2019; Riebe et al., 2003), dissolved loads carried by rivers (Gaillardet et al., 1999; J. Hartmann et al., 2014), or models coupling laboratory-derived carbonate dissolution rates and climatic and hydrological parameters such as temperature, runoff, and subsurface carbon dioxide (pCO<sub>2</sub>) levels (e.g., Calmels et al., 2014; Romero-Mujalli et al., 2019).
- (2) When using in situ cosmogenic nuclides, a bias in denudation rate determination may be introduced by the differential solubility of minerals during weathering of impure carbonate. In mixed carbonate-siliciclastic lithologies, impure carbonates are well-known features (e.g., Gunn, 1981) and recently these landscapes have received more attention with respect to cosmogenic nuclide-derived denudation rates (Bufe et al., 2022; Erlanger et al., 2021; Ott et al., 2019). The effect of silicate impurities when using only one nuclide (i.e., <sup>36</sup>Cl in calcite, or <sup>10</sup>Be in quartz) is a bias in denudation rate due to different residence times of target minerals in

soils. Ott et al. (2022) showed that this bias may be corrected for using paired  $^{36}\text{Cl}$ - $^{10}\text{Be}$  nuclide measurements.

In this study, we applied for the first time the  $^{10}\text{Be}(\text{meteoric})/^{9}\text{Be}$  cosmogenic nuclide method to a carbonate landscape. The  $^{10}\text{Be}/^{9}\text{Be}$  framework allows for the simultaneous determination of erosion and chemical weathering rates, and their sum, the denudation rate. The method does not require the presence of a certain target mineral like quartz or calcite, and it can be applied to bulk soil or sediment, or to water. This approach provides a major advantage over previous methods that need to invoke additional means to separate erosion from weathering.

Because here we present the first application of this method to a carbonate landscape we perform thorough ground-truthing of assumptions needed for carbonate lithologies, and thus employ additional analytical methods. In detail we use carbon stable isotopes to assess the contributions of stable  $^9\text{Be}$  from primary (bedrock-derived) versus secondary (re-precipitated) carbonate phases. This is necessary because secondary carbonates, precipitated from waters, contain Be released during weathering of bedrock, in contrast to non-weathered bedrock composed of primary carbonate. Further, even “pure” limestone often contains silicate impurities with much higher Be concentrations than carbonate minerals and differ strongly in their solubility from calcite or dolomite. Hence, we assess the release of  $^9\text{Be}$  during weathering from carbonate bedrock versus silicate impurities by using radiogenic strontium isotope ( $^{87}\text{Sr}/^{86}\text{Sr}$ ) ratios as a conservative source tracer, and together with elemental Be/Sr ratios, we find that a significant contribution of the Be hosted in Jura secondary carbonates is derived from the dissolution of silicates, even though the Jura limestone is considered to be very “pure.” We thoroughly evaluate different carbonate formation pathways and related sources and sinks of Be, and we include the possibility of both carbonate and silicate sources contributing Be to solutions. Thus the method is made fit for not only pure carbonate landscapes, but it should be also directly applicable to mixed siliciclastic-carbonate lithologies.

By deriving new denudation and weathering rates from both soils and sediments for the French Jura Mountains where precipitation rates exceed 1,000 mm/yr, we fill gaps in our knowledge on the controls over carbonate weathering and erosion rates.

## 2. Conceptual Framework for Deriving Erosion Rates E, Denudation Rates D, and Degrees of Weathering W in Carbonate Lithologies

### 2.1. The Original Framework

The original framework of von Blanckenburg et al. (2012) is summarized in Figure 1a and an explanation of terms can be found in Table “Notation.” In this framework, chemical weathering is tracked by the stable  $^9\text{Be}$  that is released from bedrock in the dissolved form. Dissolved Be is incorporated into so-called “reactive” phases by adsorption onto surfaces of amorphous or crystalline solids and co-precipitation during secondary solid formation in soils or rivers, or is exported in the dissolved form. A mass balance of these fluxes can be derived to reflect the partitioning of  $^9\text{Be}$  initially present in the parent bedrock ( $^9\text{Be}_{\text{parent}}$ ) into (a) the reactive phase ( $^9\text{Be}_{\text{react}}$ ), (b) the dissolved phase ( $^9\text{Be}_{\text{diss}}$ ) and (c) the silicate residual phase ( $^9\text{Be}_{\text{min}}$ ), which in terms of fluxes yields:

$$D \times [^9\text{Be}]_{\text{parent}} = E \times [^9\text{Be}]_{\text{min}} + E \times [^9\text{Be}]_{\text{react}} + q \times [^9\text{Be}]_{\text{diss}} \quad (1)$$

where square brackets denote the respective Be concentrations, D the denudation rate (in mass/area/time), E the erosion rate (same units) and q is runoff (in volume/area/time). Normalized by total Be denudation  $D \times [^9\text{Be}]_{\text{parent}}$  we obtain non-dimensional fluxes f:

$$1 = f_{\text{min}}^{^9\text{Be}} + f_{\text{react}}^{^9\text{Be}} + f_{\text{diss}}^{^9\text{Be}} \quad (2)$$

The fraction of  $^9\text{Be}$  mobilized from bedrock during weathering is  $f_{\text{react}}^{^9\text{Be}} + f_{\text{diss}}^{^9\text{Be}}$ . Because this fraction depends on the intensity to which a rock was subjected to weathering, it is a Be-specific “weathering degree.” If, as is the case in carbonate systems due to the commonly high pH in waters, most of the  $^9\text{Be}$  is partitioned into the reactive rather than the dissolved form then  $f_{\text{diss}}^{^9\text{Be}}$  is close to 0. In that case and combining Equations 1 and 2 the Be-specific weathering degree  $f_{\text{react}}^{^9\text{Be}} + f_{\text{diss}}^{^9\text{Be}}$  is:

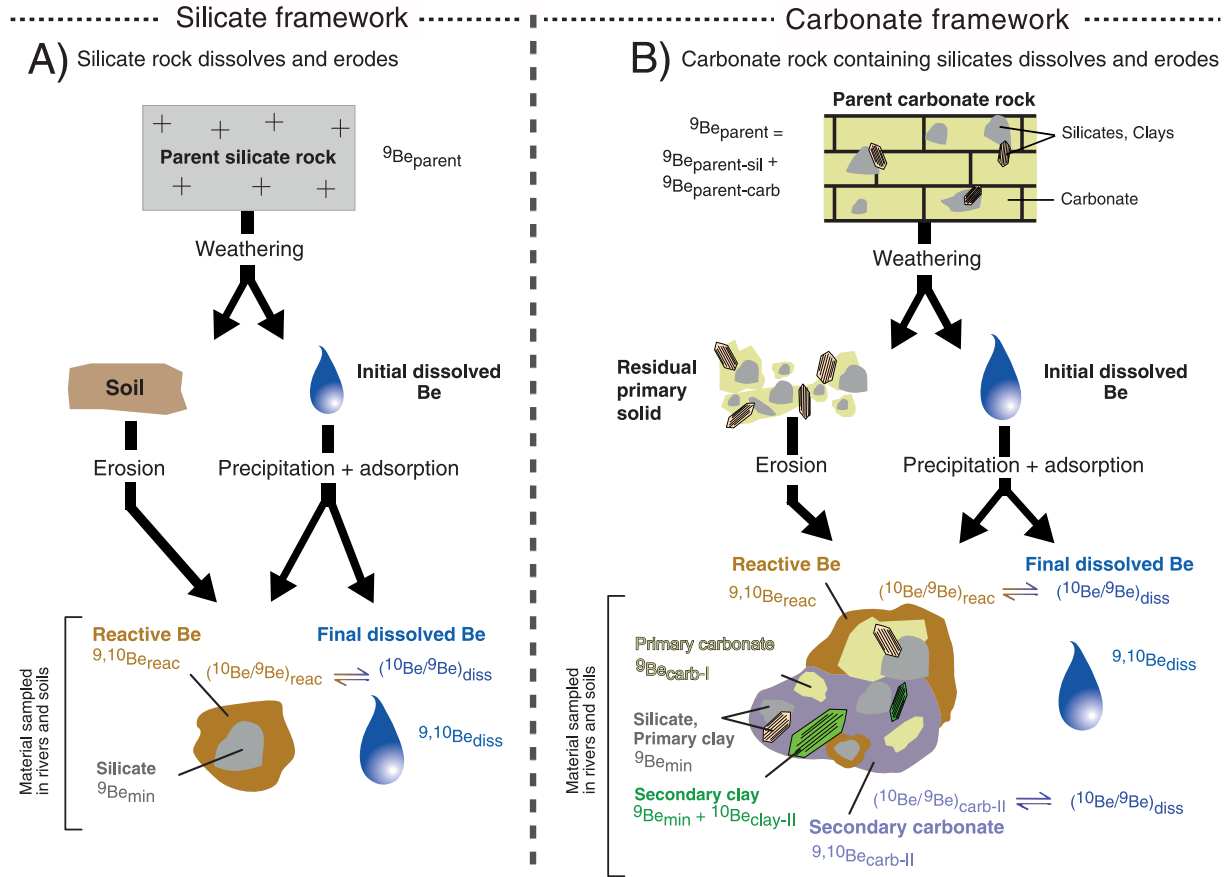


**Figure 1.** Conceptual sketch of (a) the original  ${}^{10}\text{Be}/{}^9\text{Be}$  framework developed by von Blanckenburg et al. (2012) and (b) the scenario for the framework modified for carbonate lithologies developed in this study. For calculating a denudation rate in (a) the Be from reactive solid phases that has equilibrated with Be from the dissolved phase, comprising  $[{}^{10}\text{Be}]_{\text{react}}/[{}^9\text{Be}]_{\text{react}} = ({}^{10}\text{Be}/{}^9\text{Be})_{\text{react}}$ , is considered. In (b), the phases equilibrated amongst the reactive and secondary carbonate  ${}^{10}\text{Be}$  and  ${}^9\text{Be}$  pools correspond to  $[{}^{10}\text{Be}]_{\text{react+carb-II}}/[{}^9\text{Be}]_{\text{react+carb-II}} = ({}^{10}\text{Be}/{}^9\text{Be})_{\text{react+carb-II}}$ .

$$[{}^9\text{Be}]_{\text{react}} + [{}^9\text{Be}]_{\text{diss}} = \frac{[{}^{10}\text{Be}]_{\text{react}}}{[{}^{10}\text{Be}]_{\text{react}} + [{}^9\text{Be}]_{\text{min}}} \quad (3)$$

The measurement of reactive meteoric  ${}^{10}\text{Be}$  concentrations  $[{}^{10}\text{Be}]_{\text{react}}$  (in atoms/mass), allows for the quantification of erosion rates (in mass/area/time, (Brown, 1987; Willenbring & von Blanckenburg, 2010)), provided that the depositional flux of meteoric  ${}^{10}\text{Be}$  to Earth surface,  $F^{10}\text{Be}_{\text{met}}$  (in atoms/area/time) is known and retention of  ${}^{10}\text{Be}$  to the solid phase is complete:

$$E = \frac{F_{\text{met}}^{10}\text{Be}}{[{}^{10}\text{Be}]_{\text{react}}} \quad (4)$$

As more  ${}^{10}\text{Be}$  sorbs onto fine particles with high surface area than onto coarse grains,  $[{}^{10}\text{Be}]_{\text{react}}$  depends on grain size (Willenbring & von Blanckenburg, 2010). Consequently, if a sample taken was previously sorted during for example, fluvial transport, a biased erosion rate may arise that depends on grain size (e.g., C. Shen et al., 2004; Singleton et al., 2017; Wittmann et al., 2012). The amount of  ${}^{10}\text{Be}$  hosted within the lattice of minerals (i.e., “in situ”  ${}^{10}\text{Be}$ , the “sister” nuclide of meteoric  ${}^{10}\text{Be}$ ) is generally negligible compared to reactive  ${}^{10}\text{Be}$ , such that  $[{}^{10}\text{Be}]_{\text{min}}$  does not need to be determined.

Upon release by weathering both  ${}^9\text{Be}$  and  ${}^{10}\text{Be}$  are initially present in the dissolved form, and both isotopes will be attached to reactive surfaces in proportion to their ratio in solution. The advantage of using the isotope ratio is its



independence from grain size. The Be isotope ratio ( $^{10}\text{Be}/^9\text{Be}$ ), measured in reactive ( $(^{10}\text{Be}/^9\text{Be})_{\text{reac}}$ ) phases in soils or transported as river sediment, or in the river dissolved ( $(^{10}\text{Be}/^9\text{Be})_{\text{diss}}$ ) load, then allows for estimating a denudation rate  $D$ , defined as the total chemical and erosional mass loss from a surface or catchment. With the assumption that most of the Be is partitioned into the reactive rather than the dissolved form,  $D$  (in mass/area/time) can be calculated as:

$$D = \frac{F_{\text{met}}^{10\text{Be}}}{\left(\frac{^{10}\text{Be}}{^9\text{Be}}\right)_{\text{reac/diss}} \times [^9\text{Be}]_{\text{parent}}} \times \left(f_{\text{reac}}^{9\text{Be}} + f_{\text{diss}}^{9\text{Be}}\right) \quad (5)$$

Significant incorporation of Be into a reactive phase is justified in all but low-pH settings (von Blanckenburg et al., 2012). Partition coefficients  $K_d$  describe the partitioning of an element between a solid and the dissolved phase (in volume/mass, for both  $^9\text{Be}$  and  $^{10}\text{Be}$ ):

$$K_d = \frac{[\text{Be}]_{\text{reac}}}{[\text{Be}]_{\text{diss}}} \quad (6)$$

## 2.2. The Carbonate Framework

When applied to carbonate lithologies, the silicate framework (Figure 1a) has to be adapted for four reasons:

- (1) Both carbonate and silicate minerals can contribute to  $^9\text{Be}_{\text{parent}}$  when the host rock is weathered.
- (2)  $^9\text{Be}$  and  $^{10}\text{Be}$  released during weathering are both precipitated into secondary carbonate phases, termed  $\text{Be}_{\text{carb-II}}$ .
- (3) The residual “min” phase is comprised of a silicate ( $\text{Be}_{\text{min}}$ ) and a primary carbonate ( $\text{Be}_{\text{carb-I}}$ ) component.
- (4) The silicate residual phase may contain both primary and secondary clay components (both containing  $^9\text{Be}$ ), but any  $^{10}\text{Be}$  remaining in the silicate residual fraction is of secondary clay origin.

When accounting for these reasons in the framework modified for carbonate lithologies (Figure 1b), the fraction of Be released during weathering, termed  $f_{\text{reac}}^{9\text{Be}} + f_{\text{diss}}^{9\text{Be}} = \frac{[^9\text{Be}]_{\text{reac}}}{[^9\text{Be}]_{\text{reac}} + [^9\text{Be}]_{\text{min}}}$  from Equation 3 then becomes for carbonate lithologies:

$$f_{\text{reac}}^{9\text{Be}} + f_{\text{carb}}^{9\text{Be}} = \frac{\left([^9\text{Be}]_{\text{reac}} + [^9\text{Be}]_{\text{carb-II}}\right)}{\left([^9\text{Be}]_{\text{reac}} + [^9\text{Be}]_{\text{carb-II}} + [^9\text{Be}]_{\text{min}} + [^9\text{Be}]_{\text{carb-I}}\right)} \quad (7)$$

where  $[^9\text{Be}]_{\text{carb-II}}$  is the concentration of secondary carbonate-bound  $^9\text{Be}$ , and  $[^9\text{Be}]_{\text{carb-I}}$  is the concentration of primary carbonate-bound  $^9\text{Be}$  in a soil or sediment sample.

We now explain the framework for carbonate lithologies and the derivation of Equation 7 in detail, and at the end of this section present the resulting modified equations for erosion and denudation rate calculations.

- (1) Contribution of  $^9\text{Be}$  from silicate impurities to total  $^9\text{Be}$  in carbonate parent host rocks. Both carbonate- and silicate-based Be should in principle be devoid of  $^{10}\text{Be}$ , assuming that the age of the limestone exceeds several half-lives of  $^{10}\text{Be}$  (1.4 Myr) and that the rock has not exchanged with meteoric waters since its deposition. For  $^9\text{Be}$ , however, the relative contribution of the primary carbonate ( $(^9\text{Be})_{\text{parent-carb}}$ ) and the silicate component ( $(^9\text{Be})_{\text{parent-sil}}$ ) to total  $^9\text{Be}_{\text{parent}}$

$$(^9\text{Be})_{\text{parent}} = (^9\text{Be})_{\text{parent-carb}} + (^9\text{Be})_{\text{parent-sil}} \quad (8)$$

may have to be determined by means of sequential chemical extraction. The need for sequential chemical extraction arises because weathering of limestone is likely incongruent, such that the  $^9\text{Be}$  hosted in the primary carbonate will preferentially be released over that contained in the silicate end member. How much of the  $^9\text{Be}$  hosted in silicate impurities of the parent carbonate bedrock is actually dissolving and contributing to the  $^9\text{Be}$  in solution is currently unknown. This question is particularly relevant in the context of

siliciclastic-dominated lithology with a significant carbonate component, or vice-versa, a carbonate lithology containing a significant amount of detrital silicate. In such mixed lithology cases, the contribution of two sources of  $^9\text{Be}$  (carbonate and silicate minerals) to waters (and thus also secondary carbonates) should be evaluated. Effects of fast carbonate dissolution relative to much slower release of Be from silicate phases may however be counterbalanced to some extent by the higher concentrations of  $^9\text{Be}$  in silicate (average of 2.5  $\mu\text{g/g}$  in felsic silicate rock and siliciclastic sediment; (Grew, 2002; Rudnick & Gao, 2004; Staudigel et al., 1998)) versus carbonate rocks (ranging between 0.48 and 0.68  $\mu\text{g/g}$ ; Gao et al., 1998).

We tested how much of  $^9\text{Be}$  contained in silicate impurities of the parent carbonate bedrock is released during weathering using strontium (Sr) isotope and elemental ratios in mixing calculations (see Section 3.2.2 in Wittmann et al. (2024)). This test is necessary, as even the purest limestone, like that underlying the Jura mountains, contains silicate residual, and because this test will provide a benchmark for future studies that focus on mixed lithologies. The radiogenic  $^{87}\text{Sr}/^{86}\text{Sr}$  ratio is a conservative source tracer which differs between silicate and detrital carbonate mineral end members, with strong enrichment of  $^{87}\text{Sr}$  in silicate minerals. A full Sr method description can be found in the supplement, and results are summarized in Section 4.2.3. For the following carbonate-based Be framework, it is not mandatory to know how much dissolved  $^9\text{Be}$  (and thus hosted in secondary carbonates) is derived from the dissolution of silicates.

- (2) Contribution of secondary carbonate phases that precipitate from the dissolved pool to the total reactive pool. As our chemical separation solubilizes both secondary and primary carbonate-bound Be, other methods such as carbon stable isotope ratios must be used to isolate the Be bound to secondary carbonate. During limestone weathering, secondary carbonate frequently forms in soil as carbonate nodules and near karstic springs as travertine where carbonate precipitates due to  $\text{CO}_2$  outgassing. This secondary carbonate has equilibrated with dissolved Be (both  $^9\text{Be}$  and  $^{10}\text{Be}$ ) present in soil or riverine solutions, and will incorporate dissolved Be (both  $^9\text{Be}$  and  $^{10}\text{Be}$ ) with no measurable isotope fractionation. This Be can be regarded as part of the reactive Be pool defined in our original framework (von Blanckenburg et al., 2012), independent of whether it is derived from the dissolution of primary carbonate or silicate impurities (see #1). The challenge in separating these Be pools arises in that the chemical separation of the carbonate-bound Be pool by means of acetic acid extraction (Section 3.3) is not specific to secondary carbonate phases, but will solubilize primary carbonate minerals alike. Thus, the fractions of  $^9\text{Be}$  in sediment and soils that are associated with primary ( $^9\text{Be}_{\text{carb-I}}$ ) and secondary ( $^9\text{Be}_{\text{carb-II}}$ ) carbonate phases, respectively, in the total carbonate-bound phase (termed  $^9\text{Be}_{\text{carb}}$ ) need to be determined:

$$(^9\text{Be})_{\text{carb}} = (^9\text{Be})_{\text{carb-I}} + (^9\text{Be})_{\text{carb-II}} \quad (9)$$

Deriving concentrations (in square brackets) from Equation 9 we relate to the initial total mass of soil or sediment prior to sequential extraction and digestion, called  $M_{\text{tot}}$ . Therefore:

$$[^9\text{Be}]_{\text{carb-II}} = [^9\text{Be}]_{\text{carb}} - \frac{(^9\text{Be})_{\text{carb-I}}}{M_{\text{tot}}} \quad (10)$$

where  $[^9\text{Be}]_{\text{carb-II}}$  is the concentration of the secondary carbonate-bound  $^9\text{Be}$  and  $[^9\text{Be}]_{\text{carb}}$  is the (primary plus secondary) concentration of carbonate-bound Be, both contained in the total sample mass. The concentration of primary carbonate-bound  $^9\text{Be}$  in a soil or sediment sample ( $(^9\text{Be})_{\text{carb-I}} / M_{\text{tot}}$ ) is not known, but can be obtained by measuring the concentration of carbonate-bound Be in parent rock ( $[^9\text{Be}]_{\text{parent-carb}}$ ), assuming that its composition is representative of the primary carbonate component in soil or sediment. To do this, as an intermediate step, we introduce the terms  $M_{\text{carb-I}}$  (mass of primary carbonate in a given amount of soil or sediment sample  $M_{\text{tot}}$ ) and similarly  $M_{\text{carb}}$  (mass of total carbonate, i.e. primary plus secondary in a given amount of soil or sediment sample  $M_{\text{tot}}$ ):

$$[^9\text{Be}]_{\text{carb-II}} = [^9\text{Be}]_{\text{carb}} - \frac{(^9\text{Be})_{\text{carb-I}}}{M_{\text{carb-I}}} \times \frac{M_{\text{carb-I}}}{M_{\text{carb}}} \times \frac{M_{\text{carb}}}{M_{\text{tot}}} \quad (11)$$

The ratio  $\frac{M_{\text{carb-I}}}{M_{\text{carb}}}$  in Equation 11 is the mass fraction of primary carbonate in the total carbonate mass in a soil or sediment sample, termed  $f_{\text{prim}}$ , (or  $1 - f_{\text{sec}}$ , assuming that the summed fractions of secondary ( $f_{\text{sec}}$ ) and primary carbonate equal 1). The fraction of primary carbonate in the total carbonate can be derived from for

example, carbon stable isotope ratios ( $^{13}\text{C}/^{12}\text{C}$ , i.e.  $\delta^{13}\text{C}$ ) as secondary carbonate phases (calcite) precipitating in karstic hydrosystems are expected to have a  $\delta^{13}\text{C}$  very distinct from that of the primary marine carbonate bedrock. Hence, according to mass balance,  $f_{\text{sec}}$  and  $f_{\text{prim}}$  can be calculated:

$$1 - f_{\text{sec}} = \frac{\delta^{13}\text{C}_{\text{carb}} - \delta^{13}\text{C}_{\text{carb-II}}}{\delta^{13}\text{C}_{\text{parent-carb}} - \delta^{13}\text{C}_{\text{carb-II}}} \quad (12)$$

where  $\delta^{13}\text{C}_{\text{carb-II}}$  is the expected  $\delta^{13}\text{C}$  of secondary calcite that can be estimated using Equations A5 and A6 in Wittmann et al. (2024), and  $\delta^{13}\text{C}_{\text{parent-carb}}$  and  $\delta^{13}\text{C}_{\text{carb}}$  are the  $^{13}\text{C}/^{12}\text{C}$  isotope ratios of parent bedrock and soil and sediment, respectively, assuming that  $\delta^{13}\text{C}_{\text{carb}}$  is a binary mixture between secondary calcite and primary bedrock-derived carbonate. Note that other tracers such as  $^{14}\text{C}$  or  $^{18}\text{O}$  could also be used to make this apportionment between primary and secondary carbonates.

Further, the ratio in Equation 11 is assumed to be equal to the carbonate-bound  $^9\text{Be}$  concentration of the parent source rock,  $\frac{(^9\text{Be})_{\text{parent-carb}}}{M_{\text{parent-carb}}} = [^9\text{Be}]_{\text{parent-carb}} \times \frac{M_{\text{parent-tot}}}{M_{\text{parent-carb}}}$ , such that when combining Equations 11 and 12 it follows:

$$[^9\text{Be}]_{\text{carb-II}} = [^9\text{Be}]_{\text{carb}} - \frac{M_{\text{carb}}}{M_{\text{tot}}} \times (1 - f_{\text{sec}}) \times \left( [^9\text{Be}]_{\text{parent-carb}} \times \frac{M_{\text{parent-tot}}}{M_{\text{parent-carb}}} \right) \quad (13)$$

The term  $M_{\text{carb}}/M_{\text{tot}}$  in Equation 13 accounts for the fact that  $[^9\text{Be}]_{\text{parent-carb}}$  relates to a different material ( $[^9\text{Be}]_{\text{parent-carb}}$  is measured on bedrock samples) compared to  $[^9\text{Be}]_{\text{carb-II}}$  and  $[^9\text{Be}]_{\text{carb}}$  (both measured on soil or sediment) and therefore are given relative to different total solid sample masses.

- (3) Quantification of detrital primary carbonate. According to the original framework of von Blanckenburg et al. (2012), the  $^9\text{Be}$  concentration of the residual silicate “min” fraction ( $\text{Be}_{\text{min}}$ ) has to be determined for  $^9\text{Be}$  in order to calculate the fractional flux of  $^9\text{Be}$  released by weathering. In carbonate lithologies, however, a detrital primary carbonate component may remain after weathering, containing  $^9\text{Be}$  at a concentration  $[^9\text{Be}]_{\text{carb-I}}$ . As one can measure  $[^9\text{Be}]_{\text{min}}$ ,  $[^9\text{Be}]_{\text{carb-I}}$  can be calculated as follows:

$$[^9\text{Be}]_{\text{carb-I}} = \frac{M_{\text{carb}}}{M_{\text{tot}}} \times (1 - f_{\text{sec}}) \times \left( [^9\text{Be}]_{\text{parent-carb}} \times \frac{M_{\text{parent-tot}}}{M_{\text{parent-carb}}} \right) \quad (14)$$

Using this derivation, all quantities needed to determine  $f_{\text{react}}^{9\text{Be}} + f_{\text{carb}}^{9\text{Be}}$  (Equation 7) are obtained.

- (4) Secondary clay formation. Unlike  $^9\text{Be}$ ,  $^{10}\text{Be}$  is largely absent in the silicate “min” fraction and does not need to be determined for the silicate framework. For the carbonate framework, primary carbonate-bound  $^{10}\text{Be}$  is similarly absent in all but the youngest rocks, such that  $[^{10}\text{Be}]_{\text{carb-II}} = [^{10}\text{Be}]_{\text{carb}}$ . Similarly, during limestone weathering, a secondary clay component forms and an autochthonous (original) clay component remains from bedrock. Both the primary and secondary clay components contain primary  $^9\text{Be}$ , but we have no means to quantify these relative  $^9\text{Be}$  proportions. Importantly, only the secondary clay fraction has equilibrated with dissolved Be and is assumed to obtain the same  $^{10}\text{Be}/^9\text{Be}$  as reactive and secondary carbonate Be. As both the secondary and the primary clay components are contained in the silicate residual fraction remaining after sequential extractions (Section 3.3), any  $^{10}\text{Be}$  remaining in the silicate residual fraction is of secondary clay origin, therefore termed  $^{10}\text{Be}_{\text{clay-II}}$  (note that in situ  $^{10}\text{Be}$  is negligible in comparison). Hence, for D calculations only the  $^{10}\text{Be}/^9\text{Be}$  ratio from the sum of reactive and secondary carbonate Be can be used. However, for calculations based on single  $^{10}\text{Be}$  concentrations (and not isotope ratios), such as E,  $K_d$ , and  $F_{\text{met}}^{10\text{Be}}$  calculations, all three  $^{10}\text{Be}$  components have to be taken into account:  $[^{10}\text{Be}]_{\text{react}} + [^{10}\text{Be}]_{\text{carb-II}} + [^{10}\text{Be}]_{\text{clay-II}}$  (Figure 1).

For erosion rates from meteoric  $^{10}\text{Be}$  ( $\text{t}/\text{km}^2/\text{yr}$ ), Equation 4 then is modified such that  $[^{10}\text{Be}]_{\text{carb}}$  and  $[^{10}\text{Be}]_{\text{clay-II}}$  must be added to  $[^{10}\text{Be}]_{\text{react}}$  in the denominator:

$$E = \frac{F_{\text{met}}^{10\text{Be}}}{([^{10}\text{Be}]_{\text{react}} + [^{10}\text{Be}]_{\text{carb-II}} + [^{10}\text{Be}]_{\text{clay-II}})} \quad (15)$$

When applied to carbonate lithologies Equation 5 becomes:

$$D = \frac{F_{\text{met}}^{10\text{Be}}}{\left(\frac{10\text{Be}}{9\text{Be}}\right)_{\text{react+carb-II}} \times [{}^9\text{Be}]_{\text{parent}}} \times (f_{\text{react}}^{9\text{Be}} + f_{\text{carb}}^{9\text{Be}}) \quad (16)$$

where the denudation rate  $D$  ( $\text{t}/\text{km}^2/\text{yr}$ ) is calculated assuming that both the carbonate and silicate components of the parent rock contribute to  ${}^9\text{Be}$  release to solution. Retentivity to the solid phase is efficient, as pH is high in carbonate-rich settings (see Section 4.3.2), hence no dissolved  ${}^9\text{Be}$  loss is included in Equations 15 nor 16. As shown by von Blanckenburg et al. (2012) ignoring this loss introduces only a minor bias, as  ${}^{10}\text{Be}$  is lost simultaneously and the bias only affects the  $f_{\text{react}}^{9\text{Be}} + f_{\text{carb}}^{9\text{Be}}$  term.

### 3. Study Area, Samples, and Methodology

#### 3.1. Study Area

The Jura Mountains are a NE-SW oriented fold-and-thrust belt located north of the European Alps in eastern France and north-eastern Switzerland. They represent a carbonate platform deposited in the Tethys Ocean during Jurassic-Cretaceous times, and were uplifted to an elevation of up to 1,700 m during the late stages of the Alpine collision. The main decollement accommodating the uplift zone is located at the base of a thick saline rock layer of Triassic age. Recent uplift rates range from ca. 0.2 mm/yr (Schlatter et al., 2005) to ca. 0.5 mm/yr maximum in the south-central area of the Jura (Mathey et al., 2022).

The lithology of the Jura Mountains consists of organic- and clay-poor limestone mainly composed of calcite with subordinate dolomite of Middle Jurassic (Dogger) and Upper Jurassic (Malm) ages. Two marl layers deposited during the Lower Jurassic (Lias) and the Oxfordian period form thick impermeable zones at the top of which spectacular water outflows of the well-developed karst system emerge (Calmels et al., 2014). In the Jura, large springs draining a vast underground area co-exist with smaller springs. Such smaller karst springs have more diffusive infiltration patterns where water infiltrates only into the uppermost layer, the “epikarst” layer (A. Hartmann et al., 2014). In epikarstic systems, the contribution of so-called allochthonous (soil-derived) particles to the total particulate load in the karst system is high, whereas in larger, deeper karst systems, a major contribution of the total particulate load is from insoluble silicate particles of the karstified host rock (so-called residual autochthonous clays). Deciphering their mixing and respective origins of residual solids has been attempted using rare earth element patterns (e.g., Cholet et al., 2018).

Soil depths decrease along the elevation gradient, from about 80 cm in the lowlands to about 30 cm at the highest elevation (Calmels et al., 2014; Tavant et al., 1994). Soils in the Jura are basic in pH due to the buffering by high cation concentrations (e.g., Stets et al., 2017) in mountain regions, but can actually be also slightly acidic (pH around 5) in lowland, oak-covered soils (Calmels et al., 2014). At higher altitudes, roughly along the W-E axis of Champagnole to Pontarlier, the Jura Mountains were covered by ice during the last glacial maximum (LGM or Würm period) (Ehlers & Gibbard, 2004). In our study area, the Saine and the Doubs catchment areas are located within this zone of ice cover, and the L'Angillon catchment is located at its fringes. Likely, the ice extension was more important during the previous (Riss) glacial cycle.

Climate is temperate in the French part of the Jura Mountains. Along an elevation gradient from 300 m a.s.l. to 1,200 m, mean annual temperature decreases from 11 to 5°C, mean MAP increases from 1,000 to 2,200 mm/yr and water runoff increases from 0.6 to 1.2  $\text{m}^3/\text{m}^2/\text{yr}$  (Kessler & Chambraud, 1986) (Figure 2). Modern changes in vegetation along the altitude gradient encompass a change from deciduous forest (mostly oak) at elevations below 800 m to higher elevations where human-cultivated evergreen conifers dominate. The overall dense forest cover of the Jura Mountains with mean tree stand ages of 50–60 years is a result of agricultural abandonment during the last century (Calmels et al., 2014). In central Europe, climatic conditions during the early-mid Holocene were generally somewhat wetter than today (e.g., Cheddadi et al., 1996), with a subsequent trend toward colder and drier conditions in the mid-late Holocene (e.g., Breitenbach et al., 2019). In the last millennium (specifically in the Jura), climate became more variable with a tendency to slightly wetter conditions than in earlier epochs (Magny, 1992), but generally encompassing swings from cooler and wetter conditions prior to the warmer and drier Medieval Warm Period and back to wetter conditions during the Little Ice Age. Since then, climatic



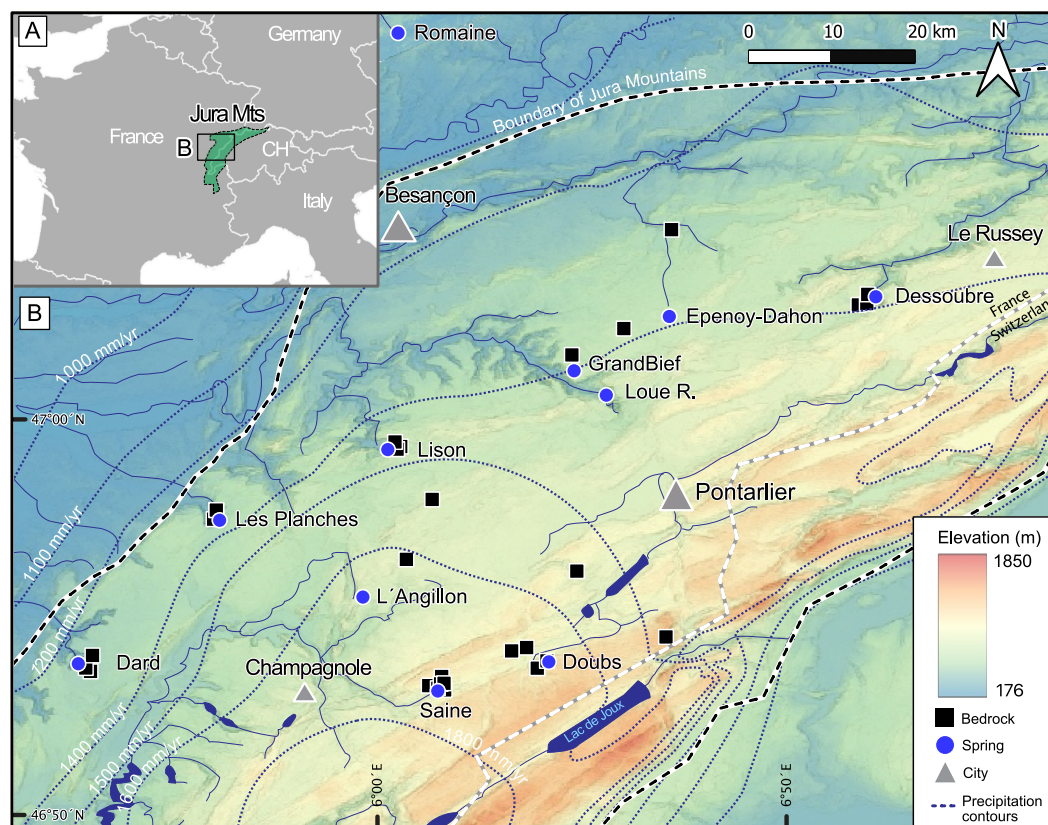


**Figure 2.** Topographic map of the study area in the French Jura Mountains with a river network and sampling points, overlain by (dotted) precipitation contour lines. In the vicinity of each spring (blue circles), water, sediment and soil samples were collected. Black squares denote bedrock samples that were mainly sampled close to springs or within each catchment. Major cities (gray triangles) are shown for reference. Loue R. = Loue River.

conditions relatively similar to today prevailed (Magny et al., 2017). These changes in climate apparently did not result in drastic vegetation patterns changes (Davis et al., 2003), as the main biome types have been temperate deciduous and cool mixed forests since the mid-late Holocene period (Davis et al., 2015). Vegetation density however likely increased, with a shift from open/less dense forest to closed, denser forests since the mid-Holocene to today (Breitenbach et al., 2019).

### 3.2. Sampling

Our samples comprising bedrock, soil, sediment, secondary carbonates (the secondary carbonate sample type is referred to as “travertine” from now on), and water roughly cover the area between Champagnole in the SW and Le Russey in the NE (Figure 2). We focused on the low-elevation Dard, Lison, Dessoubre, and L’Angillon springs, and the higher-elevation Doubs and Saine springs and their respective drainage areas for sampling. The Loue River, which is a resurgence of the Doubs, was sampled for sediment near Lods. The Romaine spring (Table A1 in Wittmann et al. (2024)) is located 40 km to the north of the Jura Mountains. We additionally sampled some smaller epikarstic springs at lower elevations, namely those of Épenoy (Dahon spring), Grand Bief in Lods, and Les Planches near Arbois (summarized as “Epikarst” in Tables and Figures).

We sampled 3–7 carbonate bedrock samples from outcrops in the drainage area of each spring, in total obtaining 29 bedrock samples, in order to constrain  $[^9\text{Be}]_{\text{parent}}$  for each spring. Prior to sampling from outcrops, the outer centimeters of bedrock were removed. For the 16 soil samples, we amalgamated several samples taken from an area of a few square meters within the drainage area of each spring, and sampled the upper 10 cm of the A-horizon (discarding the O-horizon). Further we sampled 9 sediment samples (mainly sediment that was suspended manually from the river bed or bank at each spring outlet), and 3 travertine samples from outcrops near the Dard



and Les Planches spring outlets. Solid (rocks, soil, and sediment) samples and the majority of water samples were obtained in mid-July 2017, while few other samples were collected in summer 2016. We sampled 10 different springs for water at their outlets. For two of these we obtained temporal replicates (summer 2016 and July 2017) (Table A1 in Wittmann et al. (2024)).

### 3.3. Analytical Methods

#### 3.3.1. Bedrock

Prior to crushing, a first check for secondary carbonates using UV light was done for each bedrock specimen. We used only visibly secondary carbonate-free and the center part of each specimen to exclude weathering effects. Crushed samples were powdered using a mechanical mill, and oven-dried overnight. Between 0.6 and 1.0 g were used for chemical extraction. Separation of the carbonate-bound ( ${}^9\text{Be}_{\text{parent-carb}}$ ) from the silicate-bound ( ${}^9\text{Be}_{\text{parent-sil}}$ ) Be fractions was performed following Hohl et al. (2015): Around 15 ml of 1M acetic acid was slowly added to samples. The pH was checked after bubbling subsided; in case where pH values were neutral or higher, additional 5 ml of acetic acid were added to ensure acidic pH. Samples were placed in a waterbath at 70°C for 12 hr. Samples were then centrifuged (20 min), and the supernate containing  ${}^9\text{Be}_{\text{parent-carb}}$  was filtered through PTFE syringe filters (pore size 0.45  $\mu\text{m}$ ). The residue containing  ${}^9\text{Be}_{\text{parent-sil}}$  was then fully dissolved using HF-HNO<sub>3</sub> mixtures.

Once both fractions were fully dissolved, *Inductively Coupled Plasma-Optical Emission Spectroscopy* (ICP-OES, Varian 720ES) measurements were performed using a 3M HNO<sub>3</sub> matrix for Be, and a 0.3 M HNO<sub>3</sub> matrix containing Cs for major element (Ca, Fe, Al, Ti, Zr, Mn, Na, Sr) analysis, respectively. For the carbonate-bound fraction (containing up to 10,000  $\mu\text{g/g}$  Ca), we used matrix-matched standards and a certified matrix-matched solution by SPETEC, containing 10,000  $\mu\text{g/g}$  Ca and 5 ng/g Be, as in-house standard and drift monitor to ensure bias-free Be concentration results. We re-measured about 10% of all samples ca. 2 weeks later to determine the repeatability of Be analysis and the stability of solutions under such analytically challenging conditions resulting from the high matrix load of the samples. The difference between the Be concentrations obtained from the two different OES measurements (and hence the repeatability) was  $\leq 20\%$  for Be, and did not depend on the time of measurement.

#### 3.3.2. Soil, Sediment, and Travertine

Soil samples were dried at 60°C, larger roots and leaves were removed, and samples were sieved to <2 mm. Samples were dried again at 110°C overnight and between 0.3 and 0.6 g were weighed for chemical extraction. Sediment samples were of silty texture, and were thus not sieved. Only larger (>2 mm) pebbles were removed. Travertine samples were manually powder-crushed in a mortar. For sediment and travertine, after oven-drying at 110°C overnight, about 0.3 g were used for chemical extraction. A blank and a reference soil material (“San Joaquin soil,” NIST 2709a) were processed in each batch. The latter is used to internally monitor mainly operator-dependent Be yields during extractions, as the NIST 2709a is a granitic material and is not certified for Be concentrations. Mean total  ${}^9\text{Be}$  concentrations of the NIST 2709a (the sum of all extracted fractions including “min”) are  $1.2 \pm 0.2$   $\mu\text{g/g}$  (1 sigma standard deviation, 1s; n = 3; note a long-term lab-internal mean  $\pm 1$  s is  $1.15 \pm 0.11$   $\mu\text{g/g}$ , n = 11).

We performed 3 subsequent extractions (modified mainly after Bourlès et al. (1989), Ebert et al., 2012, Hohl et al. (2015), and Wittmann et al. (2012)) using different reagents: (1) 1M acetic acid to obtain the (primary and secondary) carbonate-bound Be ( ${}^{10}\text{Be}_{\text{carb}}$  and  ${}^9\text{Be}_{\text{carb}}$ ), (2) 0.5M hydrochloric acid (HCl) to access amorphous oxides ( ${}^{10}\text{Be}_{\text{am-ox}}$  and  ${}^9\text{Be}_{\text{am-ox}}$ ), and (3) 1M hydroxylamine-hydrochloric solution to solubilize crystalline oxides ( ${}^{10}\text{Be}_{\text{x-ox}}$  and  ${}^9\text{Be}_{\text{x-ox}}$ ). After chemical extraction steps (1) and (3), residual samples were dried and weighed to infer the mass removed during each extraction step. The solid silicate residual remaining after step (3) was decomposed using hydrofluoric (HF) and aqua regia mixtures to obtain the Be bound to silicate minerals or clays ( ${}^{10}\text{Be}_{\text{min}}$  and  ${}^9\text{Be}_{\text{min}}$ ). The acetic acid extraction on soil and sediment was the same as that for bedrock samples, with the difference that due to lower sample and carbonate amounts, only 5 ml of 1M acetic acid was used. All steps following the acetic acid carbonate extraction were performed according to Wittmann et al. (2012). We term the Be contained in the sum of the amorphous and crystalline oxide phases as reactive Be ( ${}^{10}\text{Be}_{\text{reac}}$  and  ${}^9\text{Be}_{\text{reac}}$ ).

After complete dissolution of all fractions,  $^9\text{Be}$  was measured using ICP-OES in a 3M  $\text{HNO}_3$  matrix on pre-weighed splits of the leachates. For ICP-OES measurements of the carbonate-bound fraction, matrix-matched standards and a certified matrix-matched solution by SPETEC were again used (see Section 3.3.1). Major elements of all fractions were measured in a 0.3M  $\text{HNO}_3$  matrix containing Cs. Another split of the leachates was spiked with 200–300  $\mu\text{g}$  of  $^9\text{Be}$  carrier and then the Be was purified using column chemistry, alkaline precipitation and conversion to BeO following established methods (e.g., von Blanckenburg et al., 1996).  $^{10}\text{Be}$  analysis was performed by *Accelerator Mass Spectrometry* (AMS) at the ASTER National Facility (CEREGE, Aix-en-Provence, France) according to Klein et al. (2008) relative to the standard STD-11 with a nominal  $^{10}\text{Be}/^9\text{Be}$  ratio of  $(1.191 \pm 0.013) \times 10^{-11}$  (Braucher et al., 2015). We processed a total of 10 procedural blanks that yielded an average  $^{10}\text{Be}/^9\text{Be}$  ratio of  $(0.7 \pm 1.1, 1 \text{ s}) \times 10^{-15}$ , of which amounts were subtracted from sample amounts and associated uncertainties propagated.

### 3.3.3. Water

About 10 L of spring water were filtered on the day of sampling using under-pressure Teflon-coated filtration units with 0.22  $\mu\text{m}$  porosity PSE filter membranes and were thereafter immediately acidified to  $\text{pH} \leq 2$ . Water samples were then split into two aliquots, where one split (200–300 mL) was prepared for quadrupole ICP-MS (Thermo Scientific iCAP<sup>TM</sup>)  $^9\text{Be}$  analysis using standard addition methods after pre-concentration. Another split was used for  $^{10}\text{Be}$  analysis using AMS. For  $^{10}\text{Be}$  splits, 5–8 L of the “JU16” batch (see e.g. Table A1 in Wittmann et al. (2024)) and 0.5–0.8 L of all other water samples were weighed, 200–300  $\mu\text{g}$  of  $^9\text{Be}$  carrier and a  $\text{FeCl}_3$  solution were added to co-precipitate Be with ferric hydroxide (an approach adapted from Jeandel (1993) and Frank et al. (2009) developed for ocean water, see Wittmann et al. (2015) for details). After centrifugation, the precipitate was re-dissolved and then the Be was purified using column chemistry, alkaline precipitation and conversion to BeO following established methods (e.g., von Blanckenburg et al., 1996). Analysis of  $^{10}\text{Be}$  in the “JU16” water batch ( $n = 4$ ) was carried out using the AMS facility at Cologne University (Dewald et al., 2013) relative to standards KN01-6-2 and KN01-5-3, with  $^{10}\text{Be}/^9\text{Be}$  ratios of  $5.35 \times 10^{-13}$  and  $6.32 \times 10^{-12}$ , respectively. A batch-specific procedural blank with a  $^{10}\text{Be}/^9\text{Be}$  AMS ratio of  $(8.7 \pm 1.0) \times 10^{-15}$  was subtracted and uncertainties propagated. All other water samples were measured at the ASTER National Facility (see Section 3.3.2), and corrected using a total of 4 procedural blanks with an average  $^{10}\text{Be}/^9\text{Be}$  AMS ratio of only  $(0.4 \pm 0.28) \times 10^{-15}$ .

## 4. Results

### 4.1. Bedrock

#### 4.1.1. Major Element Composition of Bedrock

From major elemental analysis for rocks, molar  $(\text{Mg}/\text{Ca})_{\text{total}}$  ratios (i.e., for the total rock composition summing the “carb” and the “sil” fractions) obtained are on average 0.037, classifying the Jura bedrock as carbonate rock type, with dolomite (that would have  $\text{Mg}/\text{Ca}$  of  $>1$ ) being largely absent. The elemental composition of rocks is given in Table A2 (Wittmann et al., 2024).

#### 4.1.2. $^9\text{Be}$ Concentrations in Bedrock

The average  $[\text{}^9\text{Be}]_{\text{parent-carb}}$  is  $24 \pm 21$  ng/g (1s) for all samples, whereas the average  $[\text{}^9\text{Be}]_{\text{parent-sil}}$  fraction is  $42 \pm 27$  ng/g for all samples (see Figure 3 for values for each spring). In Figure 3 we show the average and 1s for each spring and corresponding catchment for these two fractions as well as the total (summed  $[\text{}^9\text{Be}]_{\text{parent-carb}} + [\text{}^9\text{Be}]_{\text{parent-sil}}$ )  $^9\text{Be}_{\text{parent}}$ . When averaged for each spring,  $[\text{}^9\text{Be}]_{\text{parent-carb}}$  values are ca. 30%–50% lower than  $[\text{}^9\text{Be}]_{\text{parent-sil}}$  (Figure 3). In the Dessoubre, L'Angillon, Doubs and the Epikarst sites, both  $[\text{}^9\text{Be}]_{\text{parent-carb}}$  and  $[\text{}^9\text{Be}]_{\text{parent-sil}}$  are highly variable.

### 4.2. Soil, Sediment, and Travertine

#### 4.2.1. Major Elemental Concentrations in Soil, Sediment, and Travertine

For soil, sediment, and travertine, all absolute (i.e., relative to the initial solid sample mass) concentrations of major elements are given in Table A3 and shown in Figure S1 in Wittmann et al. (2024). In the carb fraction of

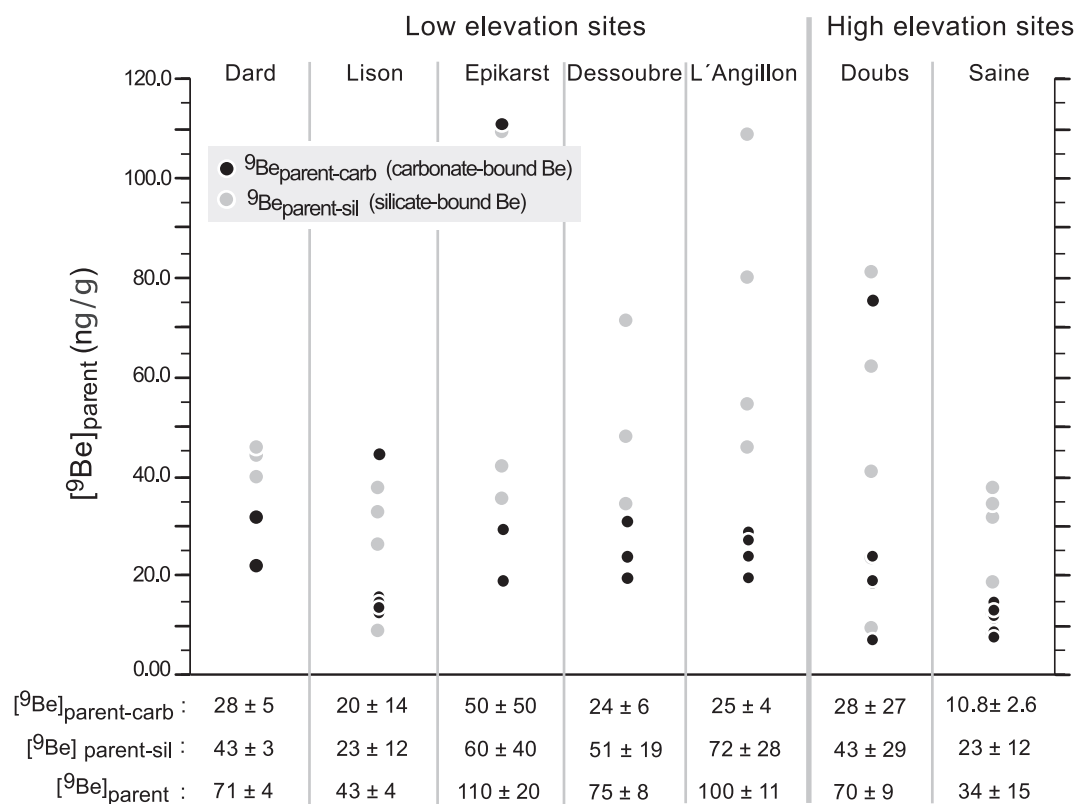


**Figure 3.**  $^9\text{Be}$  concentrations (in ng/g total sample) of the primary carbonate phase (“ $[^9\text{Be}]_{\text{parent-carb}}$ ” black symbols, extracted from powdered rocks using acetic acid), and of the silicate phase (“ $[^9\text{Be}]_{\text{parent-sil}}$ ” gray symbols, obtained from residual remaining after acetic-acid extraction) for each site. Below each site, the average  $\pm$  Std. Error is given. Epikarst sites comprise the GrandBief/Les Planches areas. The denominator mass is the initial solid sample weight (Table A2 in Wittmann et al. (2024)) in all cases. Note that there is no correlation of Be concentration with stratigraphic section age (Table A2 in Wittmann et al. (2024)).

soil, sediment, and travertine, Ca is the most abundant element, followed by Mn, Mg, and Na. Al, K, and Fe show the lowest relative contributions. The reac fraction of soils and sediments is characterized by relatively high concentrations of Fe, Mn, and Al, indicating the presence of Fe-Mn-Al-oxy-oxyhydroxides extracted during sequential leaching. Regarding the min fraction, the most abundant elements are Al (4.9, 1.9, and 1.0 wt% in soil, sediment, and travertine, respectively), Fe (3.0, 1.6, and 0.7 wt%, respectively), and K (0.6, 1, and 0.2 wt%, respectively). These elements, together with Na, comprise the main elements in the min fraction and suggest that smectite-type clay minerals were present in bedrock (see Figure S2 in Wittmann et al. (2024)). The concentrations of for example, Al, Fe, K, and Na in the min fraction of soil and sediment exceed the concentrations in bedrock by a factor of 10–20 (Tables A2 and A3 in Wittmann et al. (2024)) is due to the large fraction of calcite dissolved during weathering, thereby relatively enriching the sparingly soluble clay minerals and the elements contained therein. We also calculated the relative fractions (%) of carbonate-bound (carb), reactive (reac, sum of am-ox and x-ox), and silicate-bound (min) elemental concentrations by dividing each by the total (sum of carb, reac, and min) of elemental concentrations (Table A4 in Wittmann et al. (2024)).

#### 4.2.1.1. Comparison of Elemental Concentrations in Rock, Soil, Sediment, and Travertine

We used Al and Be elemental concentration data after normalization to Ca concentrations to compare the composition of the carbonate- and silicate-bound pools of rock, soil, sediment, and travertine (Figure 4). The low Al/Ca ratios measured in the carb fraction show that our extraction method is efficient in isolating the carbonate component of the rock, soil, and sediment samples. The fact that the carb fractions lie below the mixing array defined by the silicate residuals in the Al/Ca-Be/Ca mixing diagram indicates that while the carb fraction is devoid of Al, it still contains sizable Be, thus bound to carbonate minerals. However, the carbonate phase of soils yields Al/Ca ratios similar to those obtained from the silicate residual fraction of rocks, indicating that the carb

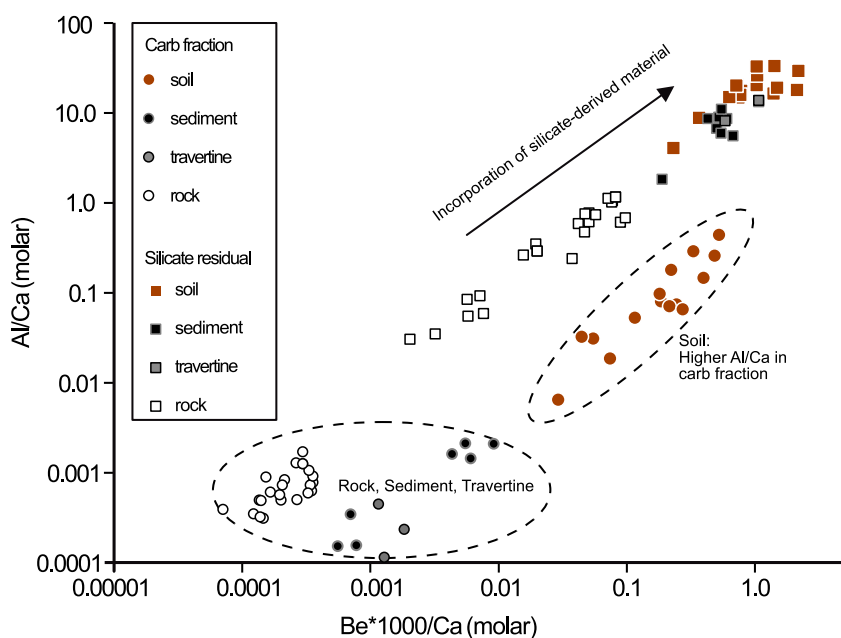


**Figure 4.** Molar Al/Ca versus Be(\*1,000)/Ca ratios for the carb (circles) and the silicate residual min (squares) fractions for rock, soil, sediment, and travertine.

extraction performed on soil samples might have partially dissolved silicate and/or oxide phases present in these samples. These fractions might carry a geochemical signal that cannot be entirely attributed to a carbonate component.

#### 4.2.2. Secondary Carbonate Contributions in Soil and Sediment and Resulting $^9\text{Be}$ Concentrations

##### 4.2.2.1. The Fraction of Secondary to Total Carbonate by Carbon Stable Isotopes

To determine how much of total (primary and secondary) carbonate is secondary carbonate, expressed as the fraction of secondary to total carbonate  $f_{\text{sec}}$ , we employed carbon stable isotopes on a subset of samples (Table A5 in Wittmann et al. (2024)). We assume that the stable carbon isotope composition of soil and sediment, termed  $\delta^{13}\text{C}_{\text{carb}}$ , is a mixture of secondary-derived carbonate precipitating from water with a carbon stable isotope composition of  $\delta^{13}\text{C}_{\text{carb-II}}$ , and primary, bedrock-derived carbonate with a carbon stable isotope composition  $\delta^{13}\text{C}_{\text{parent-carb}}$ .

Measured  $\delta^{13}\text{C}_{\text{carb}}$  are on average  $-0.8\%$  in soil and sediment and are distinctly lighter (average of  $-12.2$ ) in travertine. Bedrock- $\delta^{13}\text{C}_{\text{parent-carb}}$  is heaviest with an average of  $2.21\%$  (Table A5 in Wittmann et al. (2024)). In order to solve Equation A6 (Wittmann et al., 2024) for the stable carbon isotope composition of dissolved carbonic acid ( $\delta^{13}\text{C}_{\text{HCO}_3^-}$ ) that is needed to derive the stable carbon isotope composition of secondary calcite (Equation A5,  $\delta^{13}\text{C}_{\text{carb-II}}$ ), the  $\delta^{13}\text{C}$  of water (dissolved inorganic carbon;  $\delta^{13}\text{C}_{\text{DIC}}$ ) was also measured (ranging from  $-13.6$  to  $-16.0\%$ ; Table A5 in Wittmann et al. (2024)). Using Equation 12, we derive  $f_{\text{sec}}$  that are, as expected, highest (0.96) for travertine, indicating that these are almost exclusively composed of secondary carbonate, whereas  $f_{\text{sec}}$  values are 0.16 for soil and 0.22 for sediment on average (Table A5 in Wittmann et al. (2024)).

##### 4.2.2.2. Be Concentrations in Soil and Sediment and Proportions of Secondary Versus Primary Carbonate-Bound $^9\text{Be}$

Total  $^9\text{Be}$  concentrations ( $[^9\text{Be}]_{\text{total}}$ ), that is the sum of the “carb,” “reac,” and “min” fractions, are highest for soil (average of ca.  $1.88 \mu\text{g/g}$ ), followed by sediment (avg.  $0.78 \mu\text{g/g}$ ), whereas  $[^9\text{Be}]_{\text{total}}$  is lowest in travertine ( $0.42 \mu\text{g/g}$ ) (Figure 5a, Table A6 in Wittmann et al. (2024)). Among the individual fractions,  $[^9\text{Be}]$  are lowest for

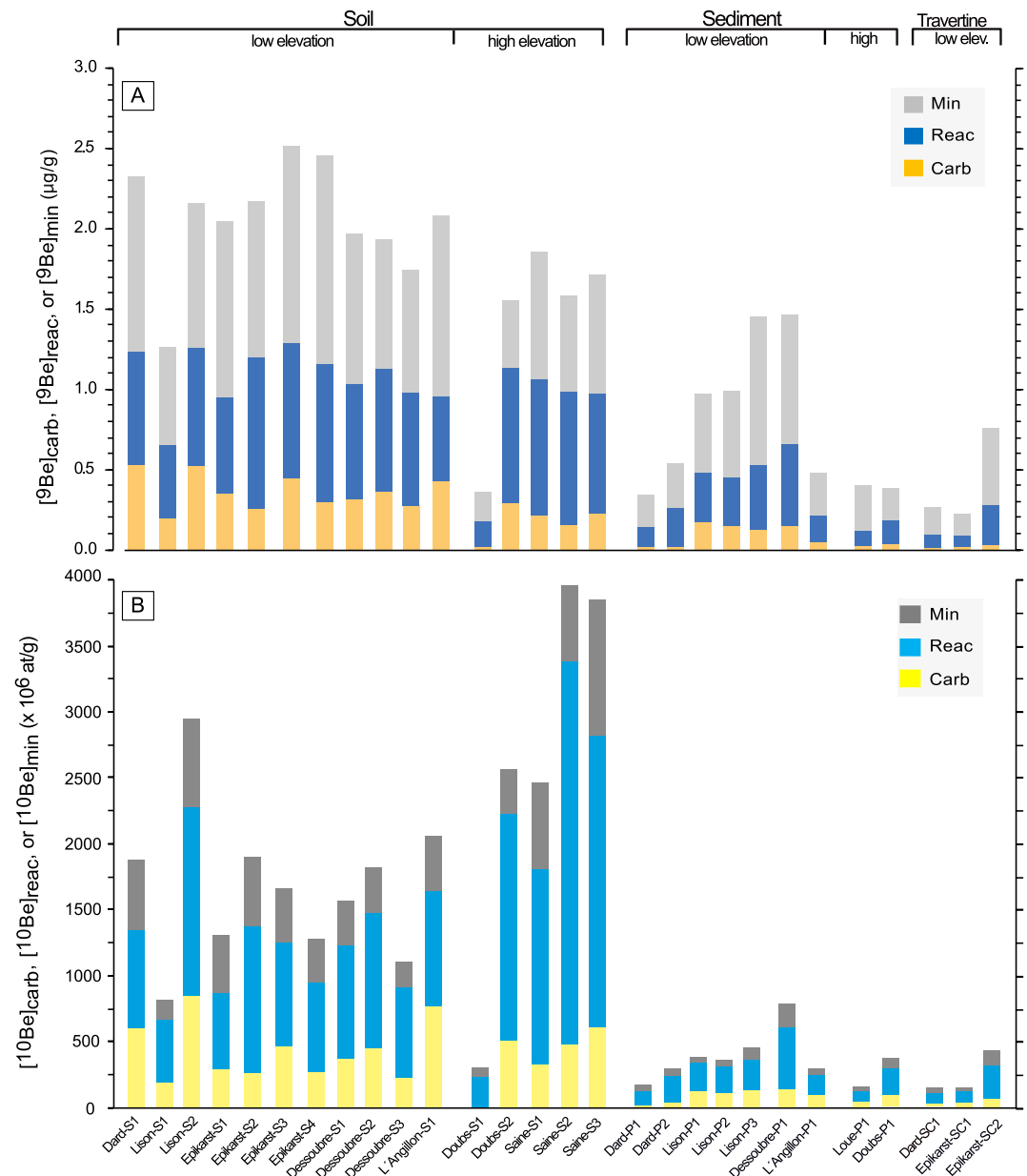


**Figure 5.** (a)  $^9\text{Be}$  concentrations ( $\mu\text{g/g}$ ) and (b)  $^{10}\text{Be}$  concentrations ( $\times 10^6 \text{ at/g}$ ) in the carbonate (“carb,” comprising both detrital primary and precipitated secondary carbonates), reactive (“reac,” sum of “am-ox” and “x-ox” leachates), and silicate residual (“min”) fractions stacked for all soil “S,” sediment “P,” and travertine “SC (Secondary Carbonate)” samples, respectively. For abbreviations see Table A1 (Wittmann et al., 2024).  $^{10}\text{Be}$  values were not obtained for the carb fraction of sample Doubs-S1. Denominator mass is the initial solid sample weight (Table A6 in Wittmann et al. (2024)) in all cases.

the extracted carbonate fraction ( $[\text{Be}]_{\text{carb}}$ , average of  $0.2 \mu\text{g/g}$ ), followed by the reactive fraction ( $[\text{Be}]_{\text{reac}}$ , average of  $0.5 \mu\text{g/g}$ ), and are highest in the residual fraction ( $[\text{Be}]_{\text{min}}$ , average of  $0.65 \mu\text{g/g}$ ).

Using the combined results from  $^9\text{Be}$  concentration data and  $f_{\text{sec}}$  (Section 4.2.2.1), we now calculate the Be concentration associated with secondary carbonate  $[\text{Be}]_{\text{carb-II}}$  (i.e., relative to the total sample mass, using Equation 13), and the Be concentration associated with primary carbonate  $[\text{Be}]_{\text{carb-I}}$  (relative to the total sample mass, Equation 14). The latter is released during the acetic acid leach, but actually comprises a part of the primary (therefore residual) carbonate that should be added to the silicate-bound Be to estimate the “min” compartment in carbonate lithologies. Results show that the Be contained in soil and travertine is almost fully comprised of



secondary carbonate-bound Be (Table A6 in Wittmann et al. (2024)). The average ratio of  $[^9\text{Be}]_{\text{carb-II}} / ([^9\text{Be}]_{\text{carb-II}} + [^9\text{Be}]_{\text{carb-I}})$  is 94%–99% for soil and travertine. On average, sediments carry a slightly lower portion of secondary carbonate-bound  $^9\text{Be}$  relative to total carbonate bound- $^9\text{Be}$  of 68%. Primary carbonate-bound  $[^9\text{Be}]_{\text{carb-I}}$  are overall low, comprising a minor fraction of total  $[^9\text{Be}]_{\text{carb}}$ , ranging between 1% and 16%. Thus, in general,  $[^9\text{Be}]_{\text{carb}} \sim [^9\text{Be}]_{\text{carb-II}}$ , and  $[^9\text{Be}]_{\text{carb-II}} \gg [^9\text{Be}]_{\text{carb-I}}$ .

#### 4.2.3. Contribution of $^9\text{Be}$ Released From Silicate Phases

The dissolution of silicates or silicate phases may contribute to the  $^9\text{Be}$  hosted in Jura secondary carbonates (and to waters). To quantify this contribution, we employed radiogenic  $^{87}\text{Sr}/^{86}\text{Sr}$ . Obtained endmembers for the silicate (min) fraction are  $(^{87}\text{Sr}/^{86}\text{Sr})_{\text{min}} = 0.7257$ , averaged from all sediment and soil samples (Table S1 in Wittmann et al. (2024)), and an endmember for primary carbonate  $(^{87}\text{Sr}/^{86}\text{Sr})_{\text{carb-I}} = 0.7072$  is averaged from the “carb” fraction of all sediment samples (Table S1 in Wittmann et al. (2024)). Note that (a) the “carb” fraction of soil contains a significant amount of silicate-derived aluminum (see Figure 4, Section 4.2.1), implying that soils have significantly different  $^{87}\text{Sr}/^{86}\text{Sr}$  ratios (Table S1 in Wittmann et al. (2024)) and are thus not used in this calculation, and (b) even though the “carb” fraction of sediment contains a relatively high fraction of secondary carbonate (Section 4.2.2.1, 22%), this contribution is ignored here. Nonetheless, the large difference of  $^{87}\text{Sr}/^{86}\text{Sr}$  between silicate and (primary) carbonate is in agreement with the assumption that  $^{87}\text{Sr}$  is strongly enriched in silicate minerals. Assuming that travertine samples were in equilibrium with the dissolved phase while being formed and comprise only secondary carbonate-bound Sr (in alignment with high  $f_{\text{sec}}$  values, Section 4.2.2.1), a binary mixing equation (Equation A2, Section 3.2.2 in Wittmann et al. (2024)) representing these end members can be solved for  $f_{\text{carb-I}}^{\text{Sr}}$ , the fraction of secondary carbonate-hosted Sr that is derived from the dissolution of primary carbonate, or, vice-versa, the fraction of Sr hosted in secondary carbonates derived from the dissolution of silicates  $(1 - f_{\text{carb-I}}^{\text{Sr}})$ .  $f_{\text{carb-I}}^{\text{Sr}}$  values range between 0.975 and 0.986 for the three travertine samples (Table S1 in Wittmann et al. (2024)), meaning that only between 1% and 3% of Sr  $(1 - f_{\text{carb-I}}^{\text{Sr}})$  hosted in secondary carbonates is derived from the dissolution of silicates. In a second step, we extend this calculation for Be, by means of elemental Be/Sr ratios, to calculate the fraction of  $^9\text{Be}$  contained in the silicate end member of the parent carbonate bedrock released during weathering,  $f_{\text{sil-diss}}^{\text{Be}}$ , using Equations A3 and A4 in Section 3.2.2 in Wittmann et al. (2024). Values of  $f_{\text{sil-diss}}^{\text{Be}}$  range between 0.27 and 0.42 for the three travertine samples. This means that, given the “purity” of the Jura limestone, a surprisingly large portion of 27%–42% (on average 33%) of the  $^9\text{Be}$  hosted in Jura secondary carbonates (and thus present in waters) is derived from the dissolution of silicates or silicate phases.

#### 4.2.4. $^{10}\text{Be}$ Concentrations in Soil, Sediment, and Travertine

Total  $^{10}\text{Be}$  concentrations ( $[^{10}\text{Be}]_{\text{total}}$ , sum of carb, reac, and clay-II fractions) are highest in soil (average of  $1,970 \times 10^6$  at/g), followed by sediment (average of  $365 \times 10^6$  at/g), and are lowest in travertine (average of  $240 \times 10^6$  at/g) (Figure 5b, Table A6 in Wittmann et al. (2024)). In contrast to  $[^9\text{Be}]$ , however, the reactive pool comprises the majority (ca. 50%–60%, i.e.,  $\sim 720 \times 10^6$  at/g) of  $[^{10}\text{Be}]_{\text{total}}$ . Carbonate- and silicate (“clay-II”)-bound  $^{10}\text{Be}$  comprise about equal shares of 20%–25% (each ca.  $280 \times 10^6$  at/g) of  $[^{10}\text{Be}]_{\text{total}}$ . This substantial  $^{10}\text{Be}_{\text{min}}$  fraction is interpreted to be firmly attached to clay minerals that existed in bedrock and that were exposed to meteoric fluids during weathering. Apparently, this fraction was not solubilized during the extractions preceding the dissolution by hydrofluoric acid. In carbonate lithologies, the  $^{10}\text{Be}$  contained in bulk carbonate phases (carb) and residual silicates (=clay-II) must thus be added to that of the reactive phase for calculation of  $E$ ,  $K_{\text{d}}$ , and  $F_{\text{met}}^{10\text{Be}}$  (Equations 6, 15, and 17).

#### 4.2.5. $^{10}\text{Be}/^9\text{Be}$ Ratios in Soil, Sediment, and Travertine

$^{10}\text{Be}/^9\text{Be}$  ratios for the different fractions ( $(^{10}\text{Be}/^9\text{Be})_{\text{carb}}$ ,  $(^{10}\text{Be}/^9\text{Be})_{\text{reac}}$ , and  $(^{10}\text{Be}/^9\text{Be})_{\text{carb+reac}}$ ) are shown in Figure 6. Note that the  $(^{10}\text{Be}/^9\text{Be})_{\text{carb+reac}}$  ratios were calculated using the sum of  $[^{10}\text{Be}]$  from total carbonate- and reactive-bound  $^{10}\text{Be}$  (Section 4.2.4), whereas  $[^9\text{Be}]$  comprises the sum of secondary carbonate- and reactive-bound  $^9\text{Be}$  (Section 4.2.2).

The  $^{10}\text{Be}/^9\text{Be}$  ratios cover a remarkably narrow range even though  $^{10}\text{Be}$  concentrations vary widely between the different fractions. Average  $^{10}\text{Be}/^9\text{Be}$  for the carb fraction are  $2.14 \times 10^{-8}$  in soil,  $2.00 \times 10^{-8}$  in sediment, and

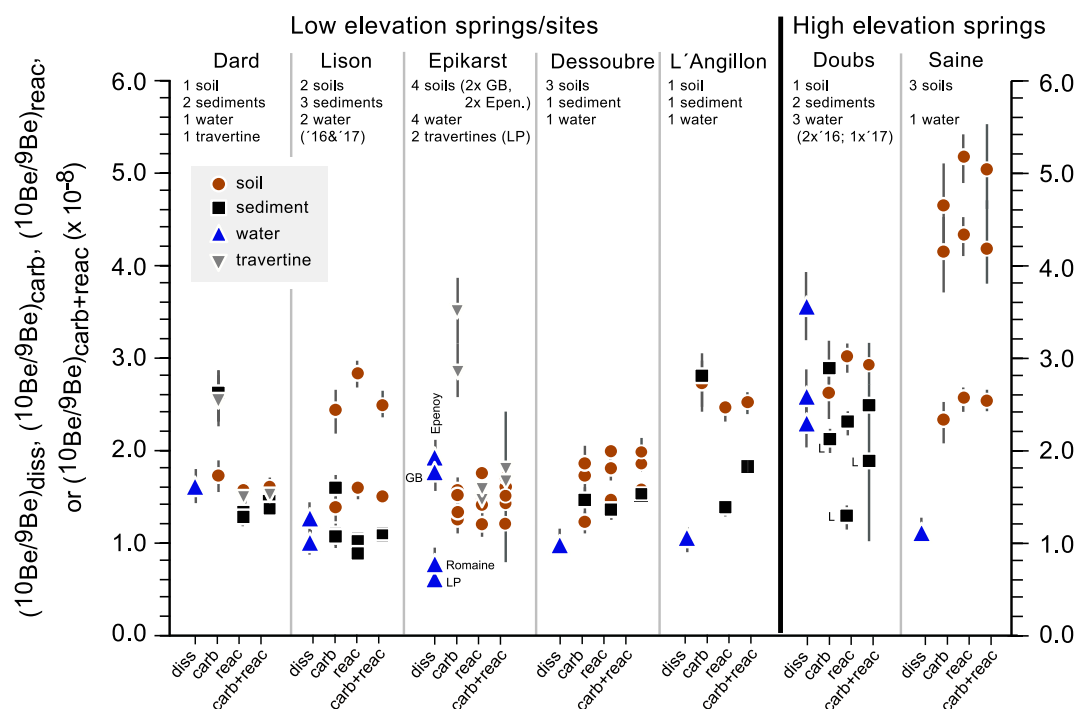


**Figure 6.**  $^{10}\text{Be}/^9\text{Be}$  ratios in soil, sediment, travertine, and spring water samples, distinguished by fraction leached (shown on the X-Axis: dissolved (diss), carbonate (carb), the reactive (reac), and the carb + reac phases). Note that the “Romaine” spring was only sampled for water and is located N of the Jura, Doubs-S1 was not added (not all fractions analyzed), GB = Grand Bief, Epen. = Epenoy-Dahon, LP = Les Planches, L = Loue-P1 fractions (Doubs resurgence; only sediment).

$3.00 \times 10^{-8}$  for travertine samples, respectively. For the reac fractions, average ratios are  $2.31 \times 10^{-8}$  in soil,  $1.29 \times 10^{-8}$  in sediment, and  $1.50 \times 10^{-8}$  in travertine, respectively, where the 1s is  $0.1\text{--}0.2 \times 10^{-8}$  for each of these fractions. Therefore, average ratios for the carb + reac fraction are  $2.3 \times 10^{-8}$  for soil,  $1.5 \times 10^{-8}$  for sediment, and  $1.7 \times 10^{-8}$  for travertine. Thus,  $^{10}\text{Be}/^9\text{Be}$  ratios among all samples and all fractions (except min-clay-II) are within a factor of only 3. Averaged over all fractions and sites,  $^{10}\text{Be}/^9\text{Be}$  ratios at the low-elevation sites are lower ( $1.2 \pm 0.7 \times 10^{-8}$ ,  $\pm 1$  s) than at the high elevation sites ( $3.4 \pm 1.1 \times 10^{-8}$ , 1 s, Figure 6).  $(^{10}\text{Be}/^9\text{Be})_{\text{min-clay-II}}$  ratios determined on the silicate residual fraction are 2.5–8 times lower than those of all other fractions, ranging from  $0.15 \times 10^{-8}$  to  $2.09 \times 10^{-8}$  with a typical 1s of  $0.03 \times 10^{-8}$  (Table A6 in Wittmann et al. (2024)).

### 4.3. Water

#### 4.3.1. $^9\text{Be}$ and $^{10}\text{Be}$ Concentrations and $^{10}\text{Be}/^9\text{Be}$ Ratios in Water Samples

$^9\text{Be}$  concentrations in water samples  $[^9\text{Be}]_{\text{diss}}$  range from 0.64 to 4.1 pg/g (on average  $1.41 \pm 0.08$  (1s) pg/g; Table A6 in Wittmann et al. (2024)). There was no trend between  $[^9\text{Be}]_{\text{diss}}$  and elevation of the springs.  $[^9\text{Be}]_{\text{diss}}$  results obtained from samples of the same springs taken in different years (Lison W2a vs. Lison W2b and Doubs W1a/b vs. Doubs W2) or from lab replicates (Doubs W1a vs. 1b) agree with each other within analytical uncertainty.  $^{10}\text{Be}$  concentrations in water samples ( $[^{10}\text{Be}]_{\text{diss}}$ , Table A6 in Wittmann et al. (2024)) range from 600 at/g (Epenoy W1) to 1,800 at/g (Saine W1). For  $[^{10}\text{Be}]_{\text{diss}}$ , low and high elevation spring samples are distinct: with  $1,000 \pm 400$  at/g ( $\pm 1$  s) the average  $[^{10}\text{Be}]_{\text{diss}}$  of low-elevation springs is significantly lower than the  $[^{10}\text{Be}]_{\text{diss}}$  of high- and low-elevation springs ( $1,600 \pm 200$  at/g).

Resulting  $(^{10}\text{Be}/^9\text{Be})_{\text{diss}}$  range from  $0.61 \times 10^{-8}$  to  $3.5 \times 10^{-8}$  (Figure 6, Table A6 in Wittmann et al. (2024)). Low-elevation springs have  $(^{10}\text{Be}/^9\text{Be})_{\text{diss}}$  ratios of  $(1.2 \pm 0.5) \times 10^{-8}$  ( $\pm 1$  s) and are lower than those of high-elevation springs ( $(^{10}\text{Be}/^9\text{Be})_{\text{diss}} = (2.0 \pm 1.0) \times 10^{-8}$ ), similar to the trend observed with sediment and soil-derived  $^{10}\text{Be}/^9\text{Be}$  ratios (Figure 6).

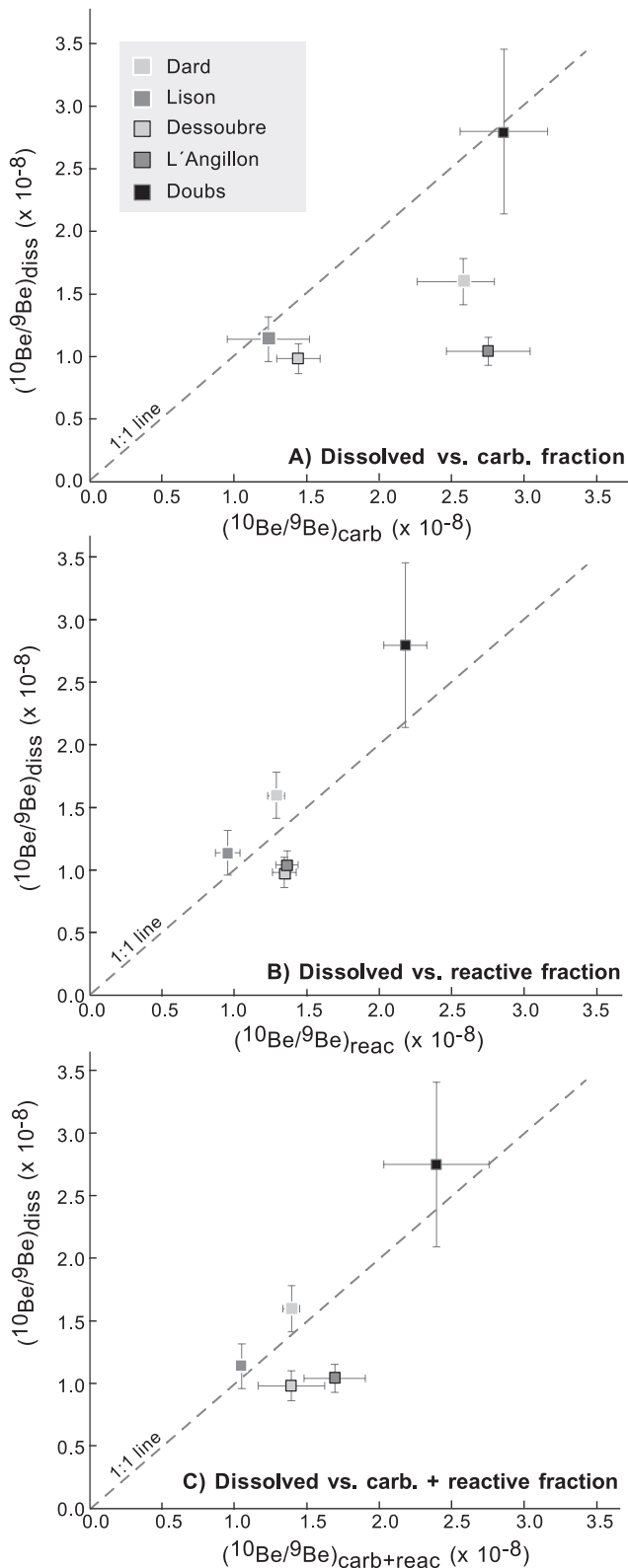


Figure 7.

We can compare  $(^{10}\text{Be}/^9\text{Be})_{\text{diss}}$  sampled from spring water to  $^{10}\text{Be}/^9\text{Be}$  ratios from sediment sampled at each spring outlet and at the same time during the field campaign in 2017 (Figure 7). Note that we did not sample soil water. Most sediment-derived  $^{10}\text{Be}/^9\text{Be}$  ratios agree with - or are slightly higher than - those of their corresponding dissolved counterpart. Notably, the  $(^{10}\text{Be}/^9\text{Be})_{\text{diss}}$  versus  $(^{10}\text{Be}/^9\text{Be})_{\text{react}}$  (Figure 7b) and  $(^{10}\text{Be}/^9\text{Be})_{\text{diss}}$  versus  $(^{10}\text{Be}/^9\text{Be})_{\text{carb+react}}$  (Figure 7c) agree better than the ratio of the dissolved versus carb. fraction (Figure 7a). For example, the analyzed  $(^{10}\text{Be}/^9\text{Be})_{\text{carb}}$  for sample Dard-P2 is about 1.5 times higher than  $(^{10}\text{Be}/^9\text{Be})_{\text{diss}}$ , but its  $(^{10}\text{Be}/^9\text{Be})_{\text{diss}}$  agrees well with  $(^{10}\text{Be}/^9\text{Be})_{\text{react}}$  and  $(^{10}\text{Be}/^9\text{Be})_{\text{carb+react}}$ , respectively (Table A6 in Wittmann et al. (2024)).

#### 4.3.2. Partition Coefficients for $^9\text{Be}$ and $^{10}\text{Be}$ Between Water and Sediment

Using the dissolved versus solid counterpart samples (sampled at the same location on the same day, i.e. water vs. sediment), we calculate partition coefficients  $K_d$  using Equation 6 modified for the carbonate framework (Table A8 in Wittmann et al. (2024)). Most log- $K_d$  values agree well for  $^9\text{Be}$  and  $^{10}\text{Be}$  and range between 5 and 5.5 for the react and carb + react fractions (Figures 8b and 8c).  $K_d$  values are lowest for the carb fraction (Figure 8a), where also  $^9\text{Be}$  and  $^{10}\text{Be}$  differ in some cases. The best agreement between log- $K_d$  values for  $^9\text{Be}$  and  $^{10}\text{Be}$  is shown for the case where we also added  $[^{10}\text{Be}]_{\text{clay-II}}$  is also added (Figure 8d).

## 5. Discussion

### 5.1. Sources and Sinks of $^9\text{Be}$ in Carbonate Landscapes

We first discuss the parent  $^9\text{Be}$  concentrations. Our average total (carb + sil)  $^9\text{Be}_{\text{parent}}$  concentration is  $\sim 70$  ng/g (Table A2 in Wittmann et al. (2024)), about  $\sim 9$  times lower than the value for carbonate rocks reported in the GERM database (<https://earthref.org>,  $0.57 \pm 0.15$   $\mu\text{g/g}$  (Gao et al., 1998)). This difference from the global database is likely due to limestones of varying degrees of purity contained in the database which highlights the need to obtain site-specific bedrock concentrations. Indeed, regarding the causes for the observed  $[^9\text{Be}]_{\text{parent}}$  variability (Figure 3), we find a significant correlation (correlation coefficient of 0.735) of  $[^9\text{Be}]_{\text{parent-sil}}$  with  $[\text{Al}]_{\text{sil}}$  (see Figure S3 in Wittmann et al. (2024)), a trend that is also apparent in Figure 4. Hence, the amount of detrital silicate phases contained in carbonate rocks might control  $[^9\text{Be}]_{\text{parent}}$  variability. We can rule out that the presence of dolomite is playing a role for  $[^9\text{Be}]_{\text{parent}}$  variability, because all rock samples have consistently low  $(\text{Mg}/\text{Ca})_{\text{total}} \ll 1$ , Table A2 in Wittmann et al. (2024)), indicating the absence of significant amounts of dolomite. Further evidence for the potential control of a silicate phase contributing Be to weathering is shown by the high (average 33%, Section 4.2.3) fraction of the  $^9\text{Be}$  hosted in Jura secondary carbonates derived from the dissolution of silicates. For a “pure” limestone setting like the Jura, we regard this value to be significant, with fractions

**Figure 7.**  $^{10}\text{Be}/^9\text{Be}$  ratios for dissolved versus sediments (sampled on same day). (a)  $(^{10}\text{Be}/^9\text{Be})_{\text{diss}}$  versus  $(^{10}\text{Be}/^9\text{Be})_{\text{carb}}$ , (b)  $(^{10}\text{Be}/^9\text{Be})_{\text{diss}}$  versus  $(^{10}\text{Be}/^9\text{Be})_{\text{react}}$ , and (c)  $(^{10}\text{Be}/^9\text{Be})_{\text{diss}}$  versus  $(^{10}\text{Be}/^9\text{Be})_{\text{carb+react}}$ .  $(^{10}\text{Be}/^9\text{Be})_{\text{carb+react}}$  ratios were calculated using the sum of  $[^{10}\text{Be}]$  from total carbonate- and reactive-bound  $^{10}\text{Be}$  (Section 4.2.4), whereas  $[^9\text{Be}]$  comprises the sum of secondary carbonate- and reactive-bound  $^9\text{Be}$  (Section 4.2.2). For the Lison, we used average values from 3 sediment samples (Table A6 in Wittmann et al. (2024)).

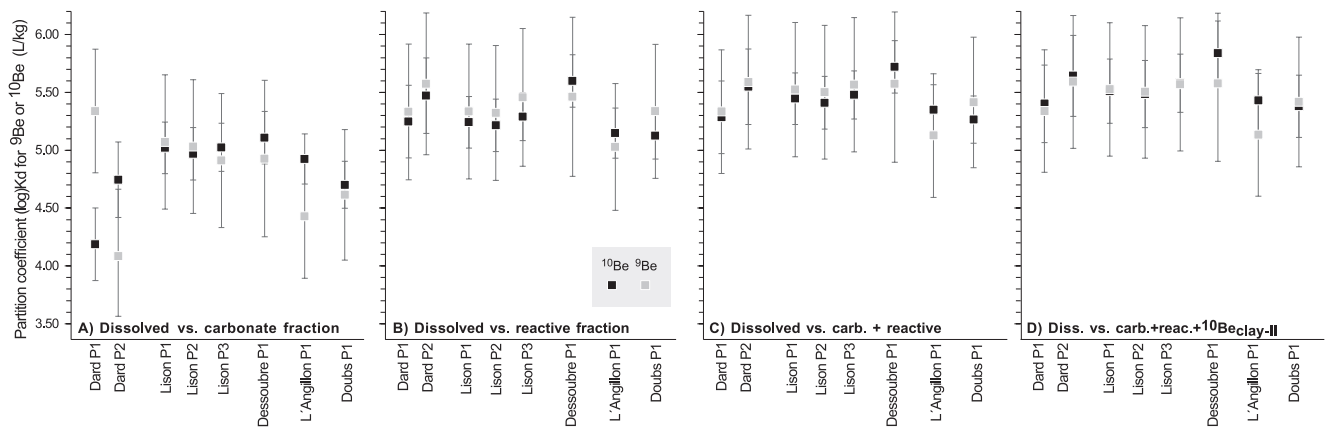


**Figure 8.** Partition coefficients ( $\log K_d$ ) calculated from  $^9\text{Be}$  and  $^{10}\text{Be}$  concentrations, respectively, for water versus sediments (sampled at same location on the same day). Soils and travertines are not shown, as these were not necessarily in physical contact with water samples. (a) Dissolved versus the carb fraction, (b) Dissolved versus the reac fraction, (c) dissolved versus the carb + reac fraction, and (d) dissolved versus the carb + reac +  $^{10}\text{Be}_{\text{clay-II}}$ . For  $^9\text{Be}$ , the carb fraction comprises the secondary carbonate fraction (carb-II) and for  $^{10}\text{Be}$ , the total carb fraction is used. In (d), the clay-II fraction is added only for  $^{10}\text{Be}$ , accounting for the fact that  $^{10}\text{Be}$  remaining in the silicate residual fraction is of secondary clay origin (Section 2.2, #4).

expected to be even higher in mixed lithologies. In consequence, (a) the silicate contribution to  $^9\text{Be}_{\text{parent}}$  must be taken into account also in pure limestone settings, that is, it is necessary to use total  $^9\text{Be}_{\text{parent}}$  from the sum of primary carbonate ( $(^9\text{Be})_{\text{parent-carb}}$ ) and the silicate-derived ( $(^9\text{Be})_{\text{parent-sil}}$ ) Be when deriving denudation rates, and (b) the approach developed in this paper should be directly applicable to all, pure and mixed, limestone and siliciclastic-limestone settings. In mixed settings with distinct lithologies, we regard it as essential to characterize  $^9\text{Be}_{\text{parent}}$  for all different rock types existing in a catchment, unless the catchment is so large that the composition of the upper continental crust can be assumed (Rahaman et al., 2017; von Blanckenburg et al., 2012; Wittmann et al., 2015).

Another aspect of the contribution of both carbonate and silicate minerals to weathering is that these minerals might have different residence times within the weathering zone as the degree of dissolution might vary with depth in the karst and solubility differ between carbonate and silicate minerals. Differences in residence times have recently been invoked for minerals of different solubilities carrying different in situ-produced cosmogenic nuclides (Ott et al., 2022). Such bias appears not to affect the  $^{10}\text{Be}/^9\text{Be}$  system:  $^{10}\text{Be}/^9\text{Be}$  ratios between the dissolved load and the carb + reac fraction of sediments are all very similar within uncertainties (Figure 7c). As water and sediment are expected to be sourced from different depths in the carbonate dissolution zone, the carbonate and the silicate reservoir appear to contribute  $^9\text{Be}$  approximately equally to the dissolved pool. Whether the sedimentary phase analyzed is dominated by particles entrained from soil (allochthonous) or by residual clay particles after rock dissolution (autochthonous) or to what degree these two components have mixed in the karst system remains unclear.

### 5.1.1. Means to Simplify the Carbonate Framework

Several options emerge to simplify the carbonate  $^{10}\text{Be}/^9\text{Be}$  framework presented in Section 2.2. First, in the Jura it appears that there is no a priori need to separate the primary from the secondary carbonate-bound  $^9\text{Be}$ . The release of  $^9\text{Be}$  during weathering of silicates and primary carbonate leads to quasi-quantitative incorporation of  $^9\text{Be}$  into secondary carbonate, meaning that the “carbonate” pool solubilized during the acetic acid extraction of sediment contains almost exclusively secondary carbonate (i.e., see Section 4.2.2  $[^9\text{Be}]_{\text{carb}} \approx [^9\text{Be}]_{\text{carb-II}}$ , and  $[^9\text{Be}]_{\text{carb-II}} \gg [^9\text{Be}]_{\text{carb-I}}$ ). Hence,  $[^9\text{Be}]_{\text{carb}}$  can be used as a faithful approximation of  $[^9\text{Be}]_{\text{carb-II}}$ , such that a determination of  $f_{\text{sec}}$  (Equations 12–14) is not needed. Second, the summed  $[^9\text{Be}]_{\text{parent}}$  ( $[^9\text{Be}]_{\text{parent-carb}} + [^9\text{Be}]_{\text{parent-sil}}$ ) can then be used to calculate denudation rates, meaning that strictly speaking, the carb- versus sil-bound pools of  $(^9\text{Be})_{\text{parent}}$  do not need to be determined separately by means of sequential chemical extraction and that a bulk decomposition suffices. However, we observe that in our research area  $[^9\text{Be}]_{\text{parent}}$  are still spatially highly variable, and overall much lower than reported in published data sets.

## 5.2. Exploring Fluid-Solid Interaction With $^9\text{Be}$ and $^{10}\text{Be}$

In this section we discuss partitioning between the solid and the dissolved phase and the correspondence between  $^{10}\text{Be}/^9\text{Be}$  ratios from sediment samples and the dissolved (spring water) phase.

Partition coefficient ( $K_d$ ) values calculated using either  $[^9\text{Be}]$  or  $[^{10}\text{Be}]$  show good agreement (Figure 8), and are largely independent of the solid Be fraction extracted from sediment that was used for calculation. Further, most  $\log(K_d)$  values exceed a value of 5 (Figure 8, Table A7 in Wittmann et al. (2024)) which is expected for pH values of around  $>7$  that were measured for most Jura spring waters (Calmels et al., 2014). Nevertheless, in detail, differences in  $K_d$  values are apparent. The  $(\log)K_d$  values for partitioning Be into the carbonate fraction (Figure 8a) are ca. 0.5 units lower than the  $(\log)K_d$  values for the reac fraction (Figure 8b). We regard it as unlikely that this is due to fast carbonate precipitation kinetics that outcompetes Be sorption as also complete Be sorption typically occurs within hours (Boschi & Willenbring, 2016; Taylor et al., 2012; You et al., 1989). The likely reason is entirely different incorporation pathways. Adsorption of  $\text{Be}(\text{OH})_2$  (or other Be molecules, see Boschi and Willenbring (2016)) onto the reac phase may play a crucial role, and will be favored by the high density of adsorption sites on reactive iron-oxhydroxide surfaces. In contrast, incorporation of Be into the carbonate-bound fraction may follow a different pathway, such as the formation of Be-carbonate complexes (Schmidbaur, 2001). The fact that Be may become a structural constituent of carbonate minerals is apparent from our Sr isotope mass balance (Section 4.2.3, details in Section 3.2.4 in Wittmann et al. (2024)) showing that Be has a high affinity for secondary carbonates, even higher than Sr.

The overall good agreement of  $(^{10}\text{Be}/^9\text{Be})_{\text{diss}}$  versus  $^{10}\text{Be}/^9\text{Be}$  measured in the reactive or secondary carbonate-bound fraction from sediment (Figure 7) shows that chemical equilibrium between  $^9\text{Be}$  and  $^{10}\text{Be}$ , as well as between dissolved and phases extracted from sediments sampled on the same day and at the same location has been attained. In detail, when comparing  $(^{10}\text{Be}/^9\text{Be})_{\text{diss}}$  versus  $(^{10}\text{Be}/^9\text{Be})_{\text{carb}}$ , about half of the  $(^{10}\text{Be}/^9\text{Be})_{\text{carb}}$  data are between 2 and 3 times higher than the corresponding  $(^{10}\text{Be}/^9\text{Be})_{\text{diss}}$ , whereas when comparing  $(^{10}\text{Be}/^9\text{Be})_{\text{diss}}$  with  $(^{10}\text{Be}/^9\text{Be})_{\text{reac}}$  (Figure 7b) or  $(^{10}\text{Be}/^9\text{Be})_{\text{carb+reac}}$  (Figure 7c), a nearly perfect agreement is observed, with a maximum difference of ca. 1.5 times. A difference of a factor of 1.5 was regarded as good agreement in previous studies (Dannhaus et al., 2018; Wittmann et al., 2015), because solids (reactive or secondary carbonate-bound phases alike) integrate over longer time scales of possibly different conditions, whereas water samples are instantaneous snapshots of modern conditions. Along the same line, the waters may have accumulated their Be at different sites than the sampled solids. In any case, the reactive reservoir plays an important role in carbonate settings. Summing the reactive and the secondary carbonate-bound Be pools provides the best means to estimate rates of denudation and weathering, consistent with previous studies (Deng et al., 2021).

## 5.3. The Depositional Flux $F^{10}\text{Be}_{\text{met}}$

For calculation of denudation and erosion rates, a prerequisite is knowledge of the depositional flux ( $F^{10}\text{Be}_{\text{met}}$ ). For all calculations in this study, the depositional flux value was read from the average of two adjacent longitudinal cells in the “mean” depositional flux map of Heikkilä and von Blanckenburg (2015). This map was generated from two global circulation model (GCM) runs that is, presents the average from one map generated for early Holocene (preindustrial) conditions, and one for industrial conditions (see Heikkilä et al., 2013; Heikkilä et al., 2014). The depositional flux from these GCMs is  $1.62 \pm 0.08 \times 10^6$  at/cm<sup>2</sup>/yr for the Jura Mountains. Note that we regard the contribution of recycled  $^{10}\text{Be}$  flux contained in dust relative to the total depositional flux to be minor in the Jura. Dust flux estimations for Central Europe range from 1 g/m<sup>2</sup>/yr at present-day (Goudie & Middleton, 2001) to 2.5 g/m<sup>2</sup>/yr for the past 5–6 Kyr to 8 g/m<sup>2</sup>/yr in the early Holocene (Le Roux et al., 2012). A presumed  $^{10}\text{Be}$  concentration of  $2.1 \times 10^8$  at/g (C. D. Shen et al., 2010) in dust would result in a dust contribution of 1.3% (present-day) to 10% (early Holocene) of the total depositional  $^{10}\text{Be}$  flux in the Jura Mountains.

We compared this GCM-derived flux to the export flux of  $^{10}\text{Be}$  measured in the Jura and used an approach similar to Deng, Wittmann, and von Blanckenburg (2020). The approach uses the total solid and dissolved river flux independently determined by D from river load gauging and the  $^{10}\text{Be}$  carried in rivers draining the Jura mountains:

$$F_{\text{met}}^{10\text{Be}} = D \times \left( \frac{[^{10}\text{Be}]}{[^9\text{Be}]} \right)_{\text{carb+reac}} \times [^9\text{Be}]_{\text{parent}} \times (f_{\text{reac}}^{9\text{Be}} + f_{\text{carb}}^{9\text{Be}}) \quad (17)$$



D in this case comprises the dissolved and suspended load-derived D from river load gauging ( $\text{kg}/\text{m}^2/\text{yr}$ , Table A8 in Wittmann et al. (2024)),  $[\text{}^{10}\text{Be}]/[\text{}^9\text{Be}]_{\text{carb+reac}}$  is the ratio of  $[\text{}^{10}\text{Be}]_{\text{carb+reac+clay-II}}$  ( $\text{at}/\text{kg}$ , Table A6 in Wittmann et al. (2024)) and  $[\text{}^9\text{Be}]_{\text{carb-II+reac}}$  ( $\text{mg}/\text{kg}$ , Table A6 in Wittmann et al. (2024)), respectively,  $[\text{}^9\text{Be}]_{\text{parent}}$  (in  $\text{mg}/\text{kg}$ ) is the sum of  $[\text{}^9\text{Be}]_{\text{parent-sil}}$  and  $[\text{}^9\text{Be}]_{\text{parent-carb}}$  (Table A2 in Wittmann et al. (2024)), and  $(f_{\text{reac}}^{\text{Be}} + f_{\text{carb}}^{\text{Be}})$  is the fraction of Be released from rock (Table A9 in Wittmann et al. (2024)). The calculated depositional flux is on average  $(1.37 \pm 0.8) \times 10^6 \text{ at}/\text{cm}^2/\text{yr}$  ( $\pm 1 \text{ s}$ ) when  $^{10}\text{Be}/^9\text{Be}$  ratios from all sediment and soil samples are used in Equation 17. If  $^{10}\text{Be}/^9\text{Be}$  ratios are sediment-derived, however, average flux values result that are lower ( $0.8 \pm 0.5 \times 10^6 \text{ at}/\text{cm}^2/\text{yr}$ ) than the average from only soils ( $1.75 \pm 0.8 \times 10^6 \text{ at}/\text{cm}^2/\text{yr}$ ) (Table A9 in Wittmann et al. (2024)). This difference may be due to grain size effects, as discussed in the next Section 5.4. Lower sediment-gauging derived depositional fluxes compared to those from the GCM agree with observations made by Deng, Wittmann, and von Blanckenburg (2020).

Another means to derive the atmospheric  $^{10}\text{Be}$  flux relies on empirical rainfall dependencies as suggested by Graly et al. (2011). Using a mean latitude of  $46.7^\circ$  and a mean annual precipitation rate of  $1,300 \text{ mm}/\text{yr}$  for low elevation and  $1,700 \text{ mm}/\text{yr}$  for high elevation Jura sites a depositional flux range of  $(2.6\text{--}3.5) \times 10^6 \text{ at}/\text{cm}^2/\text{yr}$  results, respectively. These estimates are on average a factor of 2 higher than the GCM-based fluxes. For the rates presented below we thus proceed to use the GCM-based estimate, bearing in mind that the obtained flux might also be an overestimate (Deng, Wittmann, & von Blanckenburg, 2020).

#### 5.4. Denudation, Erosion, and Weathering Rates From Meteoric $^{10}\text{Be}/^9\text{Be}$ Ratios

As an overview, we summarize denudation, erosion, and weathering rates for all soil and sediment samples averaged for low and high elevation sites in Summary Table 1, along with basic study site characteristics.

Average  $^{10}\text{Be}/^9\text{Be}$ -derived denudation rates D (Equation 16) are  $340 \pm 140$  and  $730 \pm 430 \text{ t}/\text{km}^2/\text{yr}$  (1s std. dev.) for soil and sediment, respectively (Figure 9, Table A9 in Wittmann et al. (2024)). Denudation rates from the Lison exceed these with average values of  $540$  and  $1,270 \text{ t}/\text{km}^2/\text{yr}$  for soil and sediment, respectively. Why denudation rates are so high for the Lison spring is not clear; it is the largest Jura spring in terms of discharge, draining a massive karst system, but does not have any other obvious differences to the other springs.

Meteoric  $^{10}\text{Be}$ -derived erosion rates were calculated using Equation 15. Average erosion rates are much lower when measured on soil samples ( $9.4 \pm 4.2 \text{ t}/\text{km}^2/\text{yr}$ , avg.  $\pm 1 \text{ s}$ , Summary Table 1) than those on sediment samples ( $55 \pm 28 \text{ t}/\text{km}^2/\text{yr}$ ). These clear differences result from  $[\text{}^{10}\text{Be}]$  (Figure 5b) that are much lower for sediment ( $[\text{}^{10}\text{Be}]_{\text{carb+reac+clay-II}}$  of  $(370 \pm 190) \times 10^6 \text{ at}/\text{g}$ ) than for soil ( $(2,000 \pm 1,000) \times 10^6 \text{ at}/\text{g}$ ). Soil samples are regarded to be not affected by sorting (von Blanckenburg et al., 2012), but their  $[\text{}^{10}\text{Be}]$  may still vary due to grain size distributions that differ between samples. Given our large data set of soil samples ( $n = 16$ ) that represent a variety of local conditions (i.e., sampled horizon, land use, climate, topography etc., Table A1 in Wittmann et al. (2024)) among the different soils, soil- $[\text{}^{10}\text{Be}]_{\text{carb+reac+clay-II}}$  are surprisingly uniform and thus likely represent a meaningful average for Jura soils. For sediment samples, the much lower  $[\text{}^{10}\text{Be}]$  may result from fluvial sorting that may have affected sediment samples. Correcting for riverine sorting is not a trivial task, as one would have to integrate in space (by means of river depth profiles) and time (by means of time series) in order to obtain a meaningful mean grain size that is transported by the river (e.g., Brown et al., 1988). In the Jura, data on grain size distributions are not available, but any attempt to correct for sorting will likely result in E from sediments becoming lower, not higher, if we assume that soil samples with higher  $[\text{}^{10}\text{Be}]$  than sediment comprise a more “unsorted” end member of sediment.

Considering that  $D = W + E$ , the erosion rate component in total denudation is small relative to weathering in the Jura and comprises on average only 3% of D for soil, and <7% for sediment. The remainder is considered to be a weathering rate W (i.e., calculated by  $W = D - E$ ) that encompasses all surficial and deep dissolution processes.

The resulting average W/D ratios are 0.96 and 0.92 for all soils and sediments, respectively (Summary Table 1). This means that in the pure limestone setting of the Jura Mountains, weathering fluxes represent the major portion of total denudation in soils and sediment, and any bias from sorting-affected erosion rates from sediment samples is assumed to be small. In mixed carbonate-siliciclastic settings, in contrast, physical erosion fluxes may dominate over weathering fluxes (e.g., Ott et al., 2019; Ryb et al. (2014a) and data summary in Erlanger et al. (2021)).

**Table 1**  
Summary

Elevation of spring (m)		Real catchment area (km <sup>2</sup> )	Chemical rate W	Erosion rate E	Denudation rate D	W/D	
			(t/km <sup>2</sup> /yr)				
<i>Data from gauging (Table A8)</i>							
Dard	252	225	148	3.8	152	0.97	
Lison	400	182	207	6.7	214	0.97	
Dessoubre	380	615	161	4.7	165	0.97	
Angillon	530	105	190	2.5	192	0.99	
Doubs	945	48.5	218	3.1	222	0.99	
Saine	774	56	345	4.7	350	0.99	
Sample type and number of samples for averaging		Fraction of Be released during weathering $f_{\text{Be}_{\text{reac}}}^{9\text{Be}} + f_{\text{Be}_{\text{carb}}}^{9\text{Be}}$	Chemical rate W	Erosion rate E	Denudation rate D	W/D	
			(t/km <sup>2</sup> /yr)				
<i>Data from meteoric <sup>10</sup>Be/<sup>9</sup>Be (Table A9): soil</i>							
Dard	Soil (n = 1)	0.54	390	9	400	0.97	
Lison	Soil (n = 2)	0.56	520	13	540	0.98	
Dessoubre	Soil (n = 3)	0.56	340	11	350	0.97	
Angillon	Soil (n = 1)	0.46	200	8	210	0.96	
Doubs	Soil (n = 1)	0.73	150	6.3	160	0.97	
Saine	Soil (n = 3)	0.59	330	5.0	340	0.99	
Sample type and number of samples for averaging		Fraction of Be released during weathering $f_{\text{Be}_{\text{reac}}}^{9\text{Be}} + f_{\text{Be}_{\text{carb}}}^{9\text{Be}}$	Chemical rate W	Erosion rate E	Denudation rate D	W/D	Deep weathering contribution (t/km <sup>2</sup> /yr) <sup>1</sup>
			(t/km <sup>2</sup> /yr)				
<i>Data from meteoric <sup>10</sup>Be/<sup>9</sup>Be (Table A9): sediment</i>							
Dard	Sediment (n = 2)	0.46	510	74	560	0.93	160
Lison	Sediment (n = 3)	0.44	1220	41	1280	0.95	740
Dessoubre	Sediment (n = 1)	0.45	480	21	530	0.93	180
Angillon	Sediment (n = 1)	0.46	290	55	330	0.90	120
Doubs	Sediment (n = 1)	0.48	280	44	310	0.93	150

Note. 1 Calculated from <sup>10</sup>Be/<sup>9</sup>Be-derived D(sediment) – D(soil), respectively.

The fractions of Be released during weathering ( $f_{\text{reac}}^{9\text{Be}} + f_{\text{carb}}^{9\text{Be}}$ , Equation 7) range from 0.57 to 0.44 on average for soil and sediment, respectively. Mainly the soil-derived values are higher than those previously reported for felsic landscapes from sediment samples (Figure 10). These values provide a combined weathering degree for silicates and carbonate minerals within the catchments. They reflect the almost complete dissolution of carbonate rock whilst retaining a significant amount of Be in unweathered silicates (up to 50% of Be; Figure 5a). The comparison to published data comprising only  $f_{\text{reac}}^{9\text{Be}}$  from felsic and mafic/ultramafic rocks terrains (Figure 10) shows that from a Be mass balance perspective, carbonates have  $f_{\text{reac}}^{9\text{Be}} + f_{\text{carb}}^{9\text{Be}}$  values compatible with their high solubility. A similar observation is apparent in the data sets for the Potomac River basin (Portenga et al., 2019) and the carbonate-rich Tibetan Plateau (Yang et al., 2024). Portenga et al. found higher (>0.4)  $f_{\text{reac}}^{9\text{Be}}$  values are found in areas covered by clastics, carbonates, and volcanic rocks of the Appalachian Plateau (AP), the Valley and Ridge (VR), and the Blue Ridge (BR) regions. Lowest  $f_{\text{reac}}^{9\text{Be}}$  values (ca. 0.3, Figure 10) are associated with the gneissic terrains of the Piedmont (Portenga et al., 2019), overlapping in data range with global felsic rocks. This also indicates that during

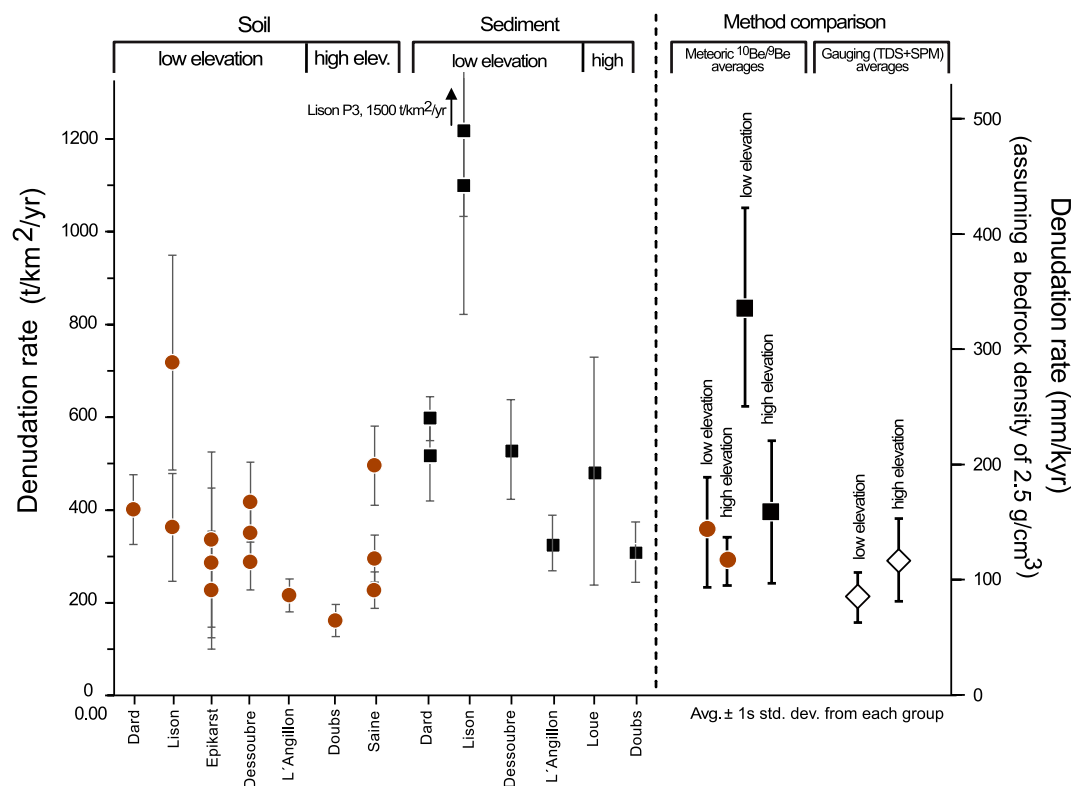


**Figure 9.** Denudation rates calculated for soil (in brown) and sediment (in black) (Equation 16, Table A9 in Wittmann et al. (2024)). The right-hand part shows the mean values for each group and the comparison with gauging-derived D (open diamonds, calculated from decadal-scale dissolved and suspended fluxes, see Table A8 in Wittmann et al. (2024)).

a reactive sequential extraction without a previous carbonate-specific leach, carbonate phases, if present, could also be solubilized.

#### 5.4.1. Soil Residence Times and Dust Input to Soils in Limestone Landscapes

To estimate upper and lower bounds of dust input into Jura soils, we combined atmospheric dust fluxes with soil residence times. To calculate soil residence times, we assume a steady state between soil production at the base of soils and soil erosion at their surface, thus dividing soil thickness by soil removal rate. In a simple scenario where all weathering takes place within the soil or regolith layer, a calculation for the Jura leads to soil residence times ranging from 5.7 to 2.1 Kyr (calculated by dividing the average soil depths of 80 cm for low-elevation soils and 30 cm for high-elevation soils, respectively, by the average soil-D of 140 mm/Kyr, that was converted from 340 t/km<sup>2</sup>/yr assuming a bedrock density of 2.5 g/cm<sup>3</sup>, Summary Table 1). However, in limestone terrains, most weathering may happen below the soil layer, while the soil layer that is mainly being composed of residual silicate particles after rock dissolution, is lowered by erosion. Hence, in an admittedly extreme, “erosion-only” endmember scenario where Jura soils are affected only by physical erosion (average erosion rate derived from meteoric <sup>10</sup>Be concentrations of 3.8 mm/Kyr, converted from a value of 9.4 t/km<sup>2</sup>/yr assuming a bedrock density of 2.5 g/cm<sup>3</sup>, Summary Table 1) results in Jura soil residence times of up to 80–210 Kyr.

However, weighted mass fractions before and after the acetic acid leach (Table A6 in Wittmann et al. (2024)) show that in the upper soil, on average, 9% of carbonate minerals may remain. This shows that weathering still takes place within the upper soils. Furthermore, given that soils may have at least partially been removed during LGM, a steady state assumption is not necessarily justified and hence these “erosion-only”-derived long residence times are overestimated.

We thus consider an intermediate post LGM- scenario with an average soil removal rate of 40 t/km<sup>2</sup>/yr that is a composite of the erosion rate (9.4 t/km<sup>2</sup>/yr) and 9% of a weathering rate ( $D - E = W$ , ~30 t/km<sup>2</sup>/yr). Note that soil

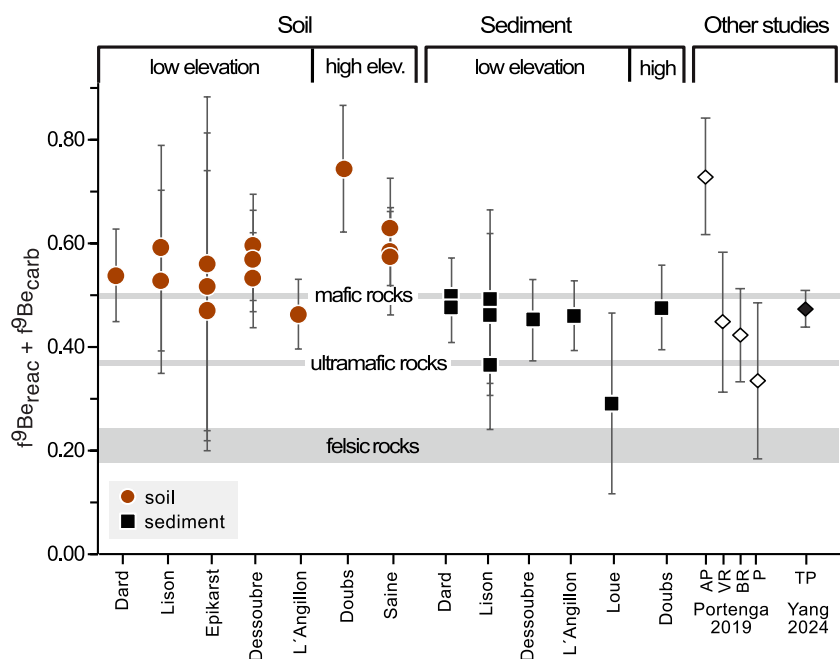


**Figure 10.** Fraction of Be released during weathering (Equation 7) for Jura soils and sediments, interpreted as Be-weathering degree, with comparison to published data. Published data comprises solely  $f^{9}\text{Be}_{\text{reac}}$  from sediment. Gray lines labeled “mafic and ultramafic rocks” data is from Dannhaus et al. (2018), and “felsic rocks” data gives the global average (von Blanckenburg & Bouchez, 2014) extended with data from the Amazon, Ganga and Bermejo basins as well as a Taiwan catchment underlain by slate (Deng, Yang, et al., 2020; Rahaman et al., 2017; Repasch et al., 2020; Wittmann et al., 2015). The right-hand part (open diamonds) shows mean values calculated from Portenga et al. (2019) for each physiographic group (AP- Appalachian Plateau, VR- Valley & Ridge, BR- Blue Ridge, P- Piedmont); closed diamond shows mean data from Yang et al. (2024) (TP-Tibetan Plateau) with uncertainty derived from the 1 s of each group.

residence times using this composite removal rate of 15 mm/Kyr (converted from 40 t/km<sup>2</sup>/yr) would be even 19–50 Kyr. If we assume that this material is supplied into soils at the same rate as a mean (present-day to late Holocene) external dust flux of ~3 g/m<sup>2</sup>/yr (equivalent to 3 t/km<sup>2</sup>/yr), the resulting dust contribution to soils may be as high as 8%. These considerations show that in regions where dust fluxes are high (e.g., Israel) and erosion rates are low, the composition of soils may be dominated by dust sources.

#### 5.4.2. Deep Versus Surficial Weathering in the Jura

A long-standing question in karst research revolves around the contribution of deep versus surficial contribution to total denudation, as solute-derived weathering rates include both components, yet they do not disclose where in the catchment mineral dissolution takes place (Bauer et al., 2005; Ford & Williams, 2007; Gabrovšek, 2009; Gunn, 2013; Kaufmann & Braun, 2000). Most work on carbonate dissolution suggests that the majority (50%–90%) occurs in the upper 10 m of soil and weathered bedrock (for a comprehensive review, see Gunn, 2013). In the Jura, spring waters are saturated with respect to calcite (saturation indices are very close to 0, see Table S3 in supplement, Wittmann et al., 2024), and Ca<sup>2+</sup> concentrations generally do not vary by more than 50% over time (Table A8 in Wittmann et al. (2024)) while runoff varies by a factor of 3–4 (Calmels et al., 2014). This oversaturation with respect to calcite indicates a coupling of carbonate weathering to acid availability and a decoupling from physical erosion (Erlanger et al., 2021). This finding is supported by the high W/D ratios (Summary Table 1) that we find for the Jura data set. Indeed, already White (1988) related the maximum denudation rate to runoff and pCO<sub>2</sub>.

The dissolution of rocks directly beneath/in soil is thought to be mainly controlled by changes in soil-pCO<sub>2</sub> driven by changes in vegetation cover and water availability, with only minor influence of temperature. For a given runoff, higher pCO<sub>2</sub> in soil under deciduous forest result in higher weathering rates for low elevation sites, and vice versa. However, Ca/Sr ratios measured in all spring waters in the Jura show large variations, in addition to pronounced differences in <sup>87</sup>Sr/<sup>86</sup>Sr ratios between the dissolved, carbonate, and silicate reservoirs (Table S1 in Wittmann et al. (2024)). Together, these observations can be explained by the precipitation of secondary

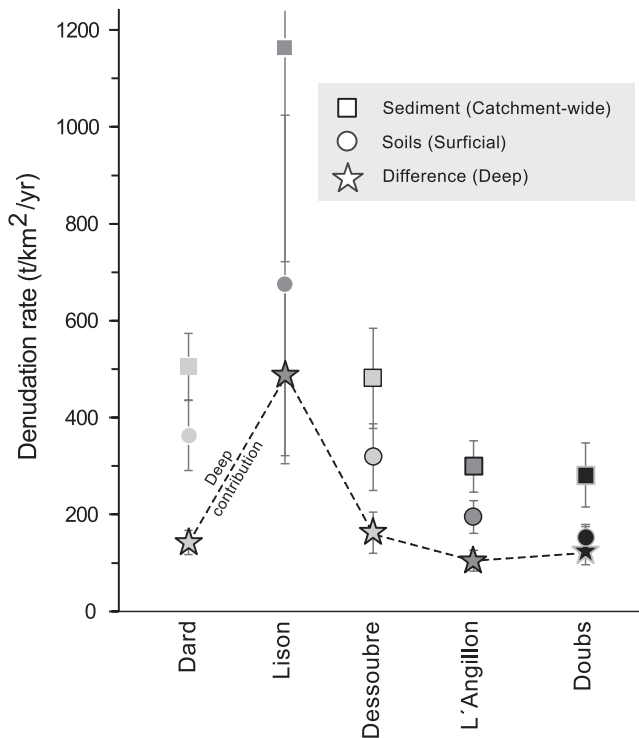


**Figure 11.**  $^{10}\text{Be}/^9\text{Be}$ -derived denudation rates  $D$  (Equation 16) for soil and sediment, and their difference, which we attribute to below-soil weathering. A deeper, below-soil weathering contribution as shown by the stippled line accounts for 30%–60% of total weathering.

carbonates and dissolution of primary silicate phases in the deep karst system that affect the Sr budget, while  $\text{Ca}^{2+}$  concentrations are unaffected (Calmels et al., 2014). Hence,  $\text{pCO}_2$  is likely set in the local soil, controlling the overall  $\text{Ca}^{2+}$  concentration of the dissolved load, while additional dissolution of carbonate and silicate minerals in the deeper karst system may not be visible in the gauging record at each spring.

From our  $^{10}\text{Be}/^9\text{Be}$ -derived denudation rates, the relative contributions of deep (i.e., below soil) versus surficial (soil) denudation of the karstic landscape can be inferred. The deeper component can be calculated from the difference between denudation rates from soil and those from sediment (stippled line in Figure 11), assuming that sediment-derived  $D$  integrate over the entire catchment, hence over both deep and surficial weathering processes, whereas soil-derived  $D$  represent only surficial weathering. An alternative sediment source, however, are allochthonous stream sediments, meaning material consisting of particles from soil that are washed into the karst and subsequently flushed through the underground karst system. In that case the sediment carries in part the  $^{10}\text{Be}/^9\text{Be}$  ratio set in soil and hence the soil-derived  $D$ . The effective sediment denudation rates would be even higher, however, because these particles would incorporate further Be that features low  $^{10}\text{Be}/^9\text{Be}$  ratios as reflected by water and sediment data (Figure 6). In any case, the minimum contribution of the deeper component to total denudation amounts to 28%–58% (Table A9 in Wittmann et al. (2024)). The minimum absolute flux of the deeper weathering amounts to 100–150  $\text{t}/\text{km}^2/\text{yr}$  across our whole sample set (except the Lison spring, where  $D$  are high throughout). Such uniform deep weathering is in agreement with ongoing dissolution in the deep karst that is unaffected by variations in vegetation and  $\text{pCO}_2$  that control weathering in surficial layers.

### 5.4.3. Comparison of Local Denudation and Weathering Rates and the Influence of Vegetation

Our average  $^{10}\text{Be}/^9\text{Be}$ -derived denudation rates are similar to decadal-scale, gauging-derived denudation rates obtained from solute measurements complemented by suspended matter concentrations from local Jura springs (Figure 9, Summary Table 1; Calmels et al. (2014)). The overall agreement between denudation rates from gauging and those from  $^{10}\text{Be}/^9\text{Be}$  is good, being within a factor of 1–2 for most of the soil and half of the sediment data, respectively.

However,  $^{10}\text{Be}/^9\text{Be}$ -denudation rates from soils agree better with rates from gauging than our  $^{10}\text{Be}/^9\text{Be}$ -denudation rates from sediment, that are on average higher than the denudation rates from soils. This can be attributed to the following potential reasons: (a)  $^{10}\text{Be}/^9\text{Be}$ -derived  $D$  from sediment is overestimated if they are subject to some yet unidentified bias. As mentioned before, the mixing of allochthonous and autochthonous particles and their re-equilibration with the dissolved  $^{10}\text{Be}/^9\text{Be}$  might set the sediment  $^{10}\text{Be}/^9\text{Be}$  ratio; (b) As also mentioned before,  $\text{Ca}^{2+}$  concentrations are thought to be mainly set in the soil due to the  $\text{pCO}_2$  at a given location, potentially controlled by vegetation type. Additional dissolution of carbonate and/or silicate phases in the deeper karst reservoir are thus not “visible” in the gauging record, but are recorded in sediment when the  $^{10}\text{Be}/^9\text{Be}$  method is employed. For the  $^{10}\text{Be}/^9\text{Be}$  system this means that when testing if a vegetation influence on weathering is present, soil-derived  $^{10}\text{Be}/^9\text{Be}$  should be employed, as sediment-derived  $^{10}\text{Be}/^9\text{Be}$  are likely less sensitive to local soil conditions. (c) A potentially large uncertainty is associated with the catchment area and the runoff variability in karst regions, as both parameters are needed to calculate gauging-derived weathering rates whilst often only poorly known in karst regions (Liu et al., 2020). In the Jura, however, the actually drained “real” catchment areas are known from for example, tracer experiments for the springs mentioned in Table A8 (Wittmann et al., 2024); (d) Similarly, combining decadal-scale dissolved  $\text{Ca}^{2+}$  fluxes from only a few sampling campaigns with suspended particulate matter concentrations that are highly variable may provide an incomplete record of denudation. Indeed, in most individual cases (also for soils) all  $^{10}\text{Be}/^9\text{Be}$ -derived  $D$  are systematically higher than  $D$  from gauging. This systematic difference is consistent with previous studies that compared millennial-scale in situ  $^{10}\text{Be}$  denudation rates measured on quartz in river sediment with denudation rates from gauging (e.g., Covault et al., 2013; Wittmann



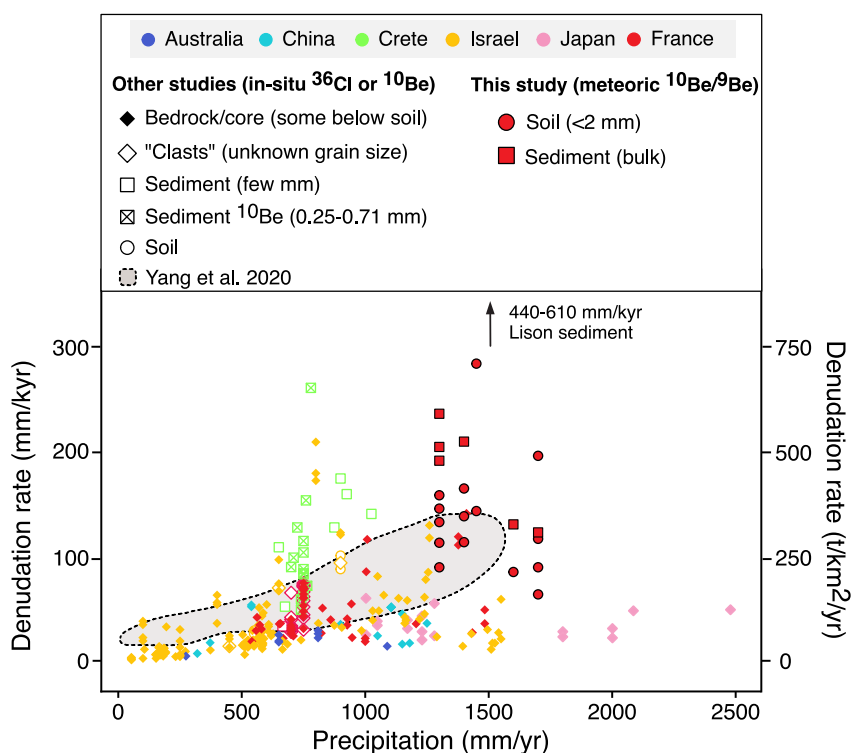


**Figure 12.** Compilation of published in situ- $^{36}\text{Cl}$ - derived denudation rates according to sample type/grain size (symbol) and study region (color) (from Ryb et al. (2014a), Ryb et al. (2014b), Matsushi et al. (2010), J. Stone et al. (1994), J. O. Stone et al. (1996), Godard et al. (2016), Yang et al. (2020), Ben-Asher et al. (2021), Avni et al. (2019), Ott et al. (2019), Thomas et al. (2018), Thomas et al. (2017), Xu et al. (2013), and Sadier et al. (2012)). Note that most of the denudation rates exceeding 100 mm/Kyr (250 t/km<sup>2</sup>/yr) were determined on sediment or weaker limestone lithologies (chalk/dolostones/flysch; Ben-Asher et al. (2021), Ott et al. (2019), and Ryb et al. (2014a)). The Crete data from Ott et al. includes in situ- $^{10}\text{Be}$  data for siliciclastic rocks (crossed green squares) for reference.

& von Blanckenburg, 2016). A common explanation is that the longer integration time of cosmogenic nuclides ensures that rare, high-magnitude erosion events are included in the measurements, while sediment gauging underestimates denudation if these events are not contained in the gauging period (Kirchner et al., 2001); (e) Intrinsic in this potential time scale bias is a change in discharge through time. If climate and/or vegetation changed (see Section 3.1), cosmogenic nuclide-derived D would also not necessarily agree with shorter-term gauging-D. Our  $^{10}\text{Be}/^9\text{Be}$ -derived D records weathering and erosion since the mid- to late Holocene where vegetation patterns remained likely largely similar to today, but how the integrative changes of a heterogeneous climate oscillating from drier to wetter and back in Europe during this period affected denudation rates relative to today is not known. Nevertheless, we regard this cause as the most likely one for the Jura, because the ratios of weathering to denudation rates (W/D) obtained from gauging agree with those from meteoric  $^{10}\text{Be}/^9\text{Be}$  mostly within 10% (Summary Table 1). This means that changes in suspended particulate matter concentrations (recording erosion, reason #4) cannot play a significant role in modifying W/D while the weathering flux comprises the major portion of total denudation. Conversely, small changes in runoff may have a big effect on W/D. Due to the different integration time scales, an agreement between gauging-D and  $^{10}\text{Be}/^9\text{Be}$ -derived D should thus not be expected.

#### 5.4.4. Meteoric-Derived Carbonate Denudation and Weathering in a Global Context

We now compare our  $^{10}\text{Be}/^9\text{Be}$ -derived D to a global compilation of  $^{36}\text{Cl}$ -derived denudation rates from mainly bedrock samples (Yang et al., 2020) in carbonate landscapes (Figure 12). We updated this compilation by including recently published work (Ben-Asher et al., 2021; Ott et al., 2019) and data from sediment samples (for grain sizes, see Figure 12). Soil data is limited to data from Ben-Asher et al. (2021), but some sampled bedrock was acknowledged to be covered by soil (Yang et al., 2020). With 150–250 mm/Kyr our denudation rates for soil and sediment from the Jura Mountains are at the upper end of the global data range. An “upper [carbonate]

denudation limit of 35 mm/Kyr" (Yang et al., 2020) was previously suggested because rates of carbonate dissolution may be kinetically limited. Our soil data exceed this limit by more than a factor of 3. Overall, our  $^{10}\text{Be}/^9\text{Be}$ -derived D peak at a MAP of 1,200–1,300 mm/yr, which coincides with the highest denudation rate values observed in Yang et al. (2020). This high denudation rate zone we marked as gray stippled area in Figure 12 following Yang et al. (2020), who also suggested that such high denudation rates may be only apparent. This was attributed to involve recent perturbations or sampling strategy, for example, because stable summits were sampled in preference over more rapidly eroding hillslopes with slopes  $>5^\circ$  (Yang et al., 2020). However, our data indicate that such high denudation rates may be common, in particular since we obtained them from sites located under temperate climate and dense vegetation cover. Notably, also our soil-derived D are in the upper range or even higher than previously determined D for this precipitation range. Thus, our data suggest that previously reported low denudation rates that were all sampled in more sparsely vegetated regions could be due to the absence in organic acids, low soil  $\text{pCO}_2$ , and overall reduced water availability that aid to decompose carbonate rocks. This is supported by Avni et al. (2019) who, although reporting lower denudation rates in a drier climate, showed a decrease in denudation rates with increasing precipitation rate. This increase was attributed to a corresponding increase in vegetation cover and thus higher soil- $\text{pCO}_2$ .

Overall, the observation that all our sediment-derived denudation rates are significantly higher than those determined from corresponding soils, attributed to a deep weathering component, suggests that a potentially significant weathering component may not only be missed by gauging records, but also by cosmogenic nuclide analyses if they are limited to bedrock, clasts, or soils.

Finally, in regions where  $\text{MAP} > 1,500\text{--}1,600$  mm/yr, our denudation rates are the first ones to be obtained from weaker non-metamorphosed carbonate rocks as opposed to those from more weathering-resistant marble (see Matsushi et al., 2010; Japan data in Figure 12) that show low denudation rates despite high MAP. Our new rates show a slight decrease in denudation rate with increasing MAP, which may support previous findings that the control of precipitation strength on denudation rate decreases at higher MAP (e.g., Yang et al., 2020).

## 6. Conclusions

The  $^{10}\text{Be}(\text{meteoric})/^9\text{Be}$  method offers a major advance for quantification of erosion rates  $E$ , weathering rates  $W$ , and denudation rates  $D$  in carbonate landscapes. The method does not require the presence of a certain target mineral for cosmogenic production such as quartz or calcite, and can be applied to bulk soil or sediment samples. It is suited to both pure limestone and mixed carbonate-siliciclastic settings. With this method, denudation rates can be determined without the need to invoke extensive and prolonged river gauging, as is the case to date.

With respect to method development, this study's most significant findings are:

- (1) We used a sequential extraction step specific for solubilizing total carbonate-bound Be using acetic acid. As this extraction cannot distinguish between secondary and primary carbonate, we employed carbon stable isotopes to obtain the fraction of Be associated with secondary carbonate. We find that  $>90\%$  of total carbonate-bound Be is bound to secondary carbonate.
- (2) Using radiogenic strontium isotope ratios, we found that about a third of the  $^9\text{Be}$  contained in secondary carbonate is derived from the dissolution of silicate phases, likely clastic impurities such as clays. These silicate phases also adsorb meteoric  $^{10}\text{Be}$  during weathering. With this additional step, the method becomes applicable to pure limestone as well as mixed carbonate-siliciclastic lithologies.
- (3) Total  $^9\text{Be}$  concentrations in bedrock are heterogeneous in the Jura, and are potentially controlled by the amount of silicate impurities contained in limestone. In limestones studies,  $^9\text{Be}_{\text{parent}}$  must be thus determined case-by-case on local bedrock.
- (4) The analysis of partition coefficients  $K_d$  between river water and secondary solids for both  $^{10}\text{Be}$  and  $^9\text{Be}$ , respectively, shows that dissolved Be has equilibrated between reactive (amorphous and crystalline Fe-oxides) and secondary carbonate phases. Secondary carbonate phases are thus part of the reactive Be pool in limestone settings.
- (5) As in previous studies in silicate lithologies  $^{10}\text{Be}$  concentrations show pronounced differences between soil and sediment samples that we attribute to grain size dependence and sorting. The  $^{10}\text{Be}/^9\text{Be}$  ratios however cover a remarkably narrow range for all samples, resulting in a narrow range in denudation rates.
- (6) The fraction of  $^9\text{Be}$  released by weathering and partitioned into secondary reactive or dissolved phases serves as a Be-specific proxy for the degree of weathering.

- (7) The atmospheric depositional flux of  $^{10}\text{Be}$  estimated for the Jura mountains from concentrations of particulate  $^{10}\text{Be}$  and river gauging is about 80% of estimates from independent global GCM-based distribution maps. The GCM estimates thus provide sufficient accuracy.

From application of these new principles, these new insights on weathering and erosion in the French Jura Mountains emerged:

The proportion of weathering in total denudation  $W/D$  is  $>0.9$ . This high proportion is due to the high purity of the limestone that almost completely dissolved. Only a small silicate mineral fraction remains that, however, carries 50% of the bedrock's  $^9\text{Be}$ . The resulting  $^{10}\text{Be}/^9\text{Be}$ -derived denudation rates are on average 340  $\text{t}/\text{km}^2/\text{yr}$  for soils and 730  $\text{t}/\text{km}^2/\text{yr}$  for river sediments. The soil-derived denudation rates agree well with previous estimates from gauging data despite their entirely different (decadal vs. millennial) integration time scales. Sediment-derived denudation rates exceed those from soil, which we attribute to a 30%–60% contribution from subsurface bedrock weathering.

On a global scale, our data provide the first cosmogenic nuclide-based denudation rates for the precipitation range of 1,200–1,700  $\text{mm}/\text{yr}$  under a temperate climate and dense vegetation cover. The resulting denudation rates exceed previous millennial-scale denudation rates from in situ- $^{36}\text{Cl}$  in calcite from less vegetated sites that do not exceed 250  $\text{t}/\text{km}^2/\text{yr}$  in this precipitation range. Our denudation rates peak (500–600  $\text{t}/\text{km}^2/\text{yr}$ ) at MAP of 1,200–1,300  $\text{mm}/\text{yr}$ . At higher MAP  $> 1,600$   $\text{mm}/\text{yr}$ , our rates then decrease to 250–350  $\text{t}/\text{km}^2/\text{yr}$ . This pattern suggests a control of precipitation on denudation/weathering that may be modulated by vegetation cover.

## Notation

Variable	Substitutions	Description	Unit	Main eq.
D		Denudation rate, sum of physical erosion and chemical weathering	$\text{kg}/\text{m}^2/\text{yr}$	5*, 16 (*silicate framework)
E		Erosion rate	$\text{kg}/\text{m}^2/\text{yr}$	4*, 15
q		Water flux	$\text{m}^3/\text{m}^2/\text{yr}$	1
$[^9\text{Be}]_{\text{parent}}$		$^9\text{Be}$ concentration in parent bedrock, rel. to total sample mass	atoms/kg	1
$[^9\text{Be}]_{\text{reac}}$		$^9\text{Be}$ concentration in the reactive phase, rel. to total sample mass	atoms/kg	1
$[^9\text{Be}]_{\text{min}}$		$^9\text{Be}$ concentration in the silicate residue, rel. to total sample mass	atoms/kg	1
$[^9\text{Be}]_{\text{diss}}$		$^9\text{Be}$ concentration in the dissolved (water) phase rel. to total water mass	atoms/L	1
$f_{\text{min}}^{^9\text{Be}}$		Fractional flux of $^9\text{Be}$ transported in primary minerals	Non-dimensional	2
$f_{\text{reac}}^{^9\text{Be}}, f_{\text{diss}}^{^9\text{Be}}$		Reactive (reac) and dissolved (diss) fractional flux of $^9\text{Be}$ released from primary minerals	Non-dimensional	2
$f_{\text{reac}}^{^9\text{Be}} + f_{\text{diss}}^{^9\text{Be}}$		Be-specific weathering degree (silicate framework)	Non-dimensional	3*
$\frac{[^9\text{Be}]_{\text{reac}}}{[^9\text{Be}]_{\text{reac}} + [^9\text{Be}]_{\text{min}}}$	$\left( \frac{[^9\text{Be}]_{\text{min}}}{[^9\text{Be}]_{\text{reac}}} + 1 \right)$	Be-specific weathering degree determined from $^9\text{Be}$ concentrations if $f_{\text{diss}}^{^9\text{Be}} = 0$	Non-dimensional	3*

<i>Continued</i>				
Variable	Substitutions	Description	Unit	Main eq.
$f_{\text{reac}}^{9\text{Be}} + f_{\text{carb}}^{9\text{Be}}$	$\frac{([^9\text{Be}]_{\text{reac}} + [^9\text{Be}]_{\text{carb-II}})}{([^9\text{Be}]_{\text{reac}} + [^9\text{Be}]_{\text{carb-II}} + [^9\text{Be}]_{\text{min}} + [^9\text{Be}]_{\text{carb-I}})}$	Be-specific weathering degree (carbonate framework) if $f_{\text{diss}}^{9\text{Be}} = 0$	Non-dimensional	7
$F_{\text{met}}^{10\text{Be}}$		Depositional flux of $^{10}\text{Be}$ to Earth's surface	atoms/m <sup>2</sup> /yr	4*, 17
$[^{10}\text{Be}]_{\text{reac}}$		Concentration of $^{10}\text{Be}$ in the reactive phase rel. to total sample mass	atoms/kg	4*, 15, 16
$[^{10}\text{Be}]_{\text{diss}}$		Concentration of $^{10}\text{Be}$ in the dissolved phase rel. to total water mass	atoms/L	
$(^{10}\text{Be}/^9\text{Be})_{\text{reac or diss}}$		Ratio of meteoric $^{10}\text{Be}$ over stable $^9\text{Be}$ in the reactive or dissolved phase	atoms/atoms	5*
$K_d$		Partition coefficient between the reactive and the dissolved phase, pH dependent	L/kg	6
$[^9\text{Be}]_{\text{parent-carb}}$		Carbonate-bound $^9\text{Be}$ concentration in host bedrock, rel. to total sample mass	atoms/kg	8
$[^9\text{Be}]_{\text{parent-sil}}$		Silicate-bound $^9\text{Be}$ concentration in host bedrock, rel. to total sample mass	atoms/kg	8
$M_{\text{tot}}$		Initial total mass of soil or sediment prior to sequential extraction and digestion	g	10, 13, 14
$M_{\text{carb}}$		Mass of total carbonate (primary plus secondary) in a given amount of soil or sediment sample $M_{\text{tot}}$	g	11, 13, 14
$M_{\text{carb-I}}$		Mass of primary carbonate in a given amount of soil or sediment sample $M_{\text{tot}}$	g	11, 13, 14
$[^9\text{Be}]_{\text{carb}}$		Total carbonate-bound (primary + secondary carbonate) $^9\text{Be}$ concentration, rel. to total sample mass	atoms/kg	9, 10
$[^9\text{Be}]_{\text{carb-I}}$		Primary carbonate-bound $^9\text{Be}$ concentration, rel. to total sample mass	atoms/kg	9, 10, 14
$[^9\text{Be}]_{\text{carb-II}}$		Secondary carbonate-bound $^9\text{Be}$ concentration, rel. to total sample mass	atoms/kg	10, 13
$f_{\text{prim}}$	$M_{\text{carb-I}}/M_{\text{carb}}; 1 - f_{\text{sec}}$	Mass fraction of primary carbonate in the total carbonate mass in a given soil or sediment sample	Non-dimensional	12

<i>Continued</i>				
Variable	Substitutions	Description	Unit	Main eq.
$f_{\text{sec}}$	$M_{\text{carb-II}}/M_{\text{carb}}; f_{\text{prim}}$	Mass fraction of secondary carbonate to total carbonate mass in a given soil or sediment sample	Non-dimensional	12
$\delta^{13}\text{C}_{\text{carb}}$		Carbon isotope composition of the inorganic carbon in sediments or soils	‰, rel. to PDB scale	12
$\delta^{13}\text{C}_{\text{carb-II}}$		Expected/calculated carbon isotope composition of secondary carbonate	‰, rel. to PDB scale	12
$\delta^{13}\text{C}_{\text{parent-carb}}$		Carbon isotope composition of the carbonate parent bedrock	‰, rel. to PDB scale	12
$M_{\text{parent-tot}}$		Initial total mass of bedrock prior to sequential extraction and digestion	g	13, 14
$M_{\text{parent-carb}}$		Mass of total carbonate (assuming primary only) in a given amount of soil or sediment sample $M_{\text{tot}}$	g	13, 14
$1 - f_{\text{carb-I}}^{\text{Sr}}$		Fraction of secondary carbonate-hosted Sr derived from the dissolution of silicates	Non-dimensional	A1, A2 (supplement)
$f_{\text{carb-I}}^{\text{Sr}}$		Fraction of secondary carbonate-hosted Sr derived from the dissolution of primary carbonate	Non-dimensional	A1, A2 (supplement)
$(^{87}\text{Sr}/^{86}\text{Sr})_{\text{carb}}$	$(^{87}\text{Sr}/^{86}\text{Sr})_{\text{carb}} = (^{87}\text{Sr}/^{86}\text{Sr})_{\text{carb-II}}$	$^{87}\text{Sr}/^{86}\text{Sr}$ ratio of the carbonate fraction of travertine (only secondary carbonate)	atoms/atoms	A1, A2 (supplement)
$(^{87}\text{Sr}/^{86}\text{Sr})_{\text{carb-I}}$		$^{87}\text{Sr}/^{86}\text{Sr}$ ratio of the fraction of primary carbonate in sediment and soil samples	atoms/atoms	A1, A2 (supplement)
$(^{87}\text{Sr}/^{86}\text{Sr})_{\text{carb-II}}$		$^{87}\text{Sr}/^{86}\text{Sr}$ ratio in the fraction of secondary carbonate in sediment and soil samples	atoms/atoms	A1, A2 (supplement)
$(^{87}\text{Sr}/^{86}\text{Sr})_{\text{min}}$		$^{87}\text{Sr}/^{86}\text{Sr}$ ratio in the silicate residual min fraction of sediment and soil samples	atoms/atoms	A1, A2 (supplement)
$f_{\text{sil-diss}}^{\text{Be}}$	$^9\text{Be}_{\text{min}}/^9\text{Be}_{\text{carb-II}}$	Fraction of $^9\text{Be}$ contained in the silicate end member of the parent carbonate bedrock released during weathering	Non-dimensional	A3, A4 (supplement)
$[^{10}\text{Be}]_{\text{carb}}$	$[^{10}\text{Be}]_{\text{carb}} = [^{10}\text{Be}]_{\text{carb-II}}$	$^{10}\text{Be}$ concentration of total carbonate phase, rel. to total sample mass	atoms/kg	15
$[^{10}\text{Be}]_{\text{clay-II}}$	$[^{10}\text{Be}]_{\text{min}}$	Concentration of $^{10}\text{Be}$ hosted within secondary clay minerals; termed “min” in silicate framework, rel. to total sample mass	atoms/kg	15



Continued				
Variable	Substitutions	Description	Unit	Main eq.
$(^{10}\text{Be}/^9\text{Be})_{\text{carb+reac}}$		Ratio of meteoric $^{10}\text{Be}$ over stable $^9\text{Be}$ in the reactive and secondary** or total carbonate phase (equilibrated with the dissolved phase). **for $^9\text{Be}$ , total for $^{10}\text{Be}$	atoms/atoms	16

## Data Availability Statement

Further supplemental information is published in an open access data publication stored in a GFZ-hosted data repository. The supplementary information contains all geochemical data obtained in this study, provided in Tables A1–A9 (Wittmann et al., 2024). The supplementary data description contains analytical procedures and data for radiogenic strontium (Table S1 in Wittmann et al. (2024)) and carbon stable isotope methods. It also contains details on the role of secondary carbonate precipitates (in addition to clays or oxides) in scavenging Be from waters (Table S2 in Wittmann et al. (2024)), as well as major element concentrations and their distribution among different samples and extracted phases (Figures S1–S3 in Wittmann et al. (2024)). The data publication is available open access at GFZ Data Services under the reference (Wittmann et al., 2024).

## Acknowledgments

We thank all participants of the “Jura 2017” field trip for help with sampling, and Marc Steinmann for discussion. This field work benefitted from the Helmholtz Research Visiting grant given to J. Gaillardet in 2017. We specifically thank L. Burtin for processing a lab batch. P. Mattern, E. Wölfer, T. Goldberg and S. Heinze are thanked for help with analyses. We acknowledge funding support by the European Research Council (ERC) grant 101055263 “Devendra”. Open Access funding enabled and organized by Projekt DEAL.

## References

- Archer, D. (2005). Fate of fossil fuel  $\text{CO}_2$  in geologic time. *Journal of Geophysical Research*, 110(C9), C09S05. <https://doi.org/10.1029/2004jc002625>
- Avni, S., Joseph-Hai, N., Haviv, I., Matmon, A., Benedetti, L., Aumaitre, G., et al. (2019). Patterns and rates of  $10^3$ – $10^5$  yr denudation in carbonate terrains under subhumid to subalpine climatic gradient, Mount Hermon, Israel. *Geological Society of America Bulletin*, 131(5–6), 899–912. <https://doi.org/10.1130/b31973.1>
- Bakalowicz, M. (2015). Karst and karst groundwater resources in the Mediterranean. *Environmental Earth Sciences*, 74(1), 5–14. <https://doi.org/10.1007/s12665-015-4239-4>
- Bauer, S., Liedl, R., & Sauter, M. (2005). Modeling the influence of epikarst evolution on karst aquifer genesis: A time-variant recharge boundary condition for joint karst-epikarst development. *Water Resources Research*, 41(9), W09416. <https://doi.org/10.1029/2004WR003321>
- Beaulieu, E., Goddérís, Y., Donnadiou, Y., Labat, D., & Roelandt, C. (2012). High sensitivity of the continental-weathering carbon dioxide sink to future climate change. *Nature Climate Change*, 2(5), 346–349. <https://doi.org/10.1038/nclimate1419>
- Ben-Asher, M., Haviv, I., Crouvi, O., Roering, J. J., & Matmon, A. (2021). The convexity of carbonate hilltops:  $^{36}\text{Cl}$  constraints on denudation and chemical weathering rates and implications for hillslope curvature. *GSA Bulletin*, 133(9–10), 1930–1946. <https://doi.org/10.1130/b35658.1>
- Ben-Asher, M., Haviv, I., Roering, J. J., & Crouvi, O. (2019). The potential influence of dust flux and chemical weathering on hillslope morphology: Convex soil-mantled carbonate hillslopes in the Eastern Mediterranean. *Geomorphology*, 341, 203–215. <https://doi.org/10.1016/j.geomorph.2019.05.021>
- Bierman, P. R., & Nichols, K. K. (2004). Rock to sediment—Slope to sea with  $^{10}\text{Be}$ —Rates of landscape change. *Annual Review of Earth and Planetary Sciences*, 32(1), 215–255. <https://doi.org/10.1146/annurev.32.101802.120539>
- Binet, S., Probst, J. L., Batiot, C., Seidel, J. L., Emblanch, C., Peyraube, N., et al. (2020). Global warming and acid atmospheric deposition impacts on carbonate dissolution and  $\text{CO}_2$  fluxes in French karst hydrosystems: Evidence from hydrochemical monitoring in recent decades. *Geochimica et Cosmochimica Acta*, 270, 184–200. <https://doi.org/10.1016/j.gca.2019.11.021>
- Boschi, V., & Willenbring, J. (2016). The effect of pH, organic ligand chemistry and mineralogy on the sorption of beryllium over time. *Environmental Chemistry*, 13(4), 711. <https://doi.org/10.1071/en15107>
- Bourlès, D., Raisbeck, G. M., & Yiou, F. (1989).  $^{10}\text{Be}$  and  $^9\text{Be}$  in marine sediments and their potential for dating. *Geochimica et Cosmochimica Acta*, 53(2), 443–452. [https://doi.org/10.1016/0016-7037\(89\)90395-5](https://doi.org/10.1016/0016-7037(89)90395-5)
- Braucher, R., Guillou, V., Bourlès, D. L., Arnold, M., Aumaitre, G., Keddadouche, K., & Nottoli, E. (2015). Preparation of ASTER in-house  $^{10}\text{Be}/^9\text{Be}$  standard solutions. *Nuclear Instruments and Methods in Physics Research Section B: Beam Interactions with Materials and Atoms*, 361, 335–340. <https://doi.org/10.1016/j.nimb.2015.06.012>
- Breitenbach, S. F. M., Plessen, B., Waltgenbach, S., Tjallingii, R., Leonhardt, J., Jochum, K. P., et al. (2019). Holocene interaction of maritime and continental climate in Central Europe: New speleothem evidence from Central Germany. *Global and Planetary Change*, 176, 144–161. <https://doi.org/10.1016/j.gloplacha.2019.03.007>
- Brown, L. (1987).  $^{10}\text{Be}$  as a tracer of erosion and sediment transport. *Chemical Geology*, 65(3–4), 189–196. [https://doi.org/10.1016/0168-9622\(87\)90002-9](https://doi.org/10.1016/0168-9622(87)90002-9)
- Brown, L., Pavich, M., Hickman, R. E., Klein, J., & Middleton, R. (1988). Erosion of the Eastern United States observed with  $^{10}\text{Be}$ . *Earth Surface Processes and Landforms*, 13(5), 441–457. <https://doi.org/10.1002/esp.3290130509>
- Bufe, A., Cook, K. L., Galy, A., Wittmann, H., & Hovius, N. (2022). The effect of lithology on the relationship between denudation rate and chemical weathering pathways—Evidence from the eastern Tibetan Plateau. *Earth Surface Dynamics*, 10(3), 513–530. <https://doi.org/10.5194/esurf-10-513-2022>
- Bufe, A., Hovius, N., Emberson, R., Rugenstein, J. K. C., Galy, A., Hassenruck-Gudipati, H. J., & Chang, J.-M. (2021). Co-variation of silicate, carbonate and sulfide weathering drives  $\text{CO}_2$  release with erosion. *Nature Geoscience*, 14(4), 211–216. <https://doi.org/10.1038/s41561-021-00714-3>

- Bufe, A., Rugenstein, J. K. C., & Hovius, N. (2024). CO<sub>2</sub> drawdown from weathering is maximized at moderate erosion rates. *Science*, 383(6687), 1075–1080. <https://doi.org/10.1126/science.adk0957>
- Calmels, D., Gaillardet, J., Brenot, A., & France-Lanord, C. (2007). Sustained sulfide oxidation by physical erosion processes in the Mackenzie River basin: Climatic perspectives. *Geology*, 35(11), 1003–1006. <https://doi.org/10.1130/g24132a.1>
- Calmels, D., Gaillardet, J., & François, L. (2014). Sensitivity of carbonate weathering to soil CO<sub>2</sub> production by biological activity along a temperate climate transect. *Chemical Geology*, 390, 74–86. <https://doi.org/10.1016/j.chemgeo.2014.10.010>
- Cheddadi, R., Yu, G., Guiot, J., Harrison, S. P., & Prentice, I. C. (1996). The climate of Europe 6000 years ago. *Climate Dynamics*, 13(1), 1–9. <https://doi.org/10.1007/s003820050148>
- Cholet, C., Steinmann, M., Charlier, J.-B., & Denimal, S. (2018). Characterizing fluxes of trace metals related to dissolved and suspended matter during a storm event: Application to a karst aquifer using trace metals and rare Earth elements as provenance indicators. *Hydrogeology Journal*, 27(1), 305–319. <https://doi.org/10.1007/s10040-018-1859-2>
- Covault, J. A., Craddock, W. H., Romans, B. W., Fildani, A., & Gosai, M. (2013). Spatial and temporal variations in landscape evolution: Historic and longer-term sediment flux through global catchments. *The Journal of Geology*, 121(1), 35–56. <https://doi.org/10.1086/668680>
- Dannhaus, N., Wittmann, H., Krám, P., Christl, M., & von Blanckenburg, F. (2018). Catchment-wide weathering and erosion rates of mafic, ultramafic, and granitic rock from cosmogenic meteoric <sup>10</sup>Be/<sup>9</sup>Be ratios. *Geochimica et Cosmochimica Acta*, 222, 618–641. <https://doi.org/10.1016/j.gca.2017.11.005>
- Davis, B. A. S., Brewer, S., Stevenson, A. C., & Guiot, J. (2003). The temperature of Europe during the Holocene reconstructed from pollen data. *Quaternary Science Reviews*, 22(15–17), 1701–1716. [https://doi.org/10.1016/s0277-3791\(03\)00173-2](https://doi.org/10.1016/s0277-3791(03)00173-2)
- Davis, B. A. S., Collins, P. M., & Kaplan, J. O. (2015). The age and post-glacial development of the modern European vegetation: A plant functional approach based on pollen data. *Vegetation History and Archaeobotany*, 24(2), 303–317. <https://doi.org/10.1007/s00334-014-0476-9>
- Deng, K., Wittmann, H., & von Blanckenburg, F. (2020). The depositional flux of meteoric cosmogenic <sup>10</sup>Be from modeling and observation. *Earth and Planetary Science Letters*, 550, 116530. <https://doi.org/10.1016/j.epsl.2020.116530>
- Deng, K., Wittmann, H., Yang, S. L., & von Blanckenburg, F. (2021). The upper limit of denudation rate measurement from cosmogenic <sup>10</sup>Be (meteoric)<sup>9</sup>Be ratios in Taiwan. *Journal of Geophysical Research: Earth Surface*, 126(10), e2021JF006221. <https://doi.org/10.1029/2021jf006221>
- Deng, K., Yang, S., von Blanckenburg, F., & Wittmann, H. (2020). Denudation rate changes along a fast-eroding mountainous river with slate headwaters in Taiwan from <sup>10</sup>Be(Meteoritic)<sup>9</sup>Be ratios. *Journal of Geophysical Research: Earth Surface*, 125(2), e2019JF005251. <https://doi.org/10.1029/2019jf005251>
- Dewald, A., Heinze, S., Jolie, J., Zilges, A., Dunai, T., Rethemeyer, J., et al. (2013). CologneAMS, a dedicated center for accelerator mass spectrometry in Germany. *Nuclear Instruments and Methods in Physics Research Section B: Beam Interactions with Materials and Atoms*, 294(0), 18–23. <https://doi.org/10.1016/j.nimb.2012.04.030>
- Dong, X., Cohen, M. J., Martin, J. B., McLaughlin, D. L., Murray, A. B., Ward, N. D., et al. (2019). Ecohydrologic processes and soil thickness feedbacks control limestone-weathering rates in a karst landscape. *Chemical Geology*, 527, 118774. <https://doi.org/10.1016/j.chemgeo.2018.05.021>
- Ebert, K., Willenbring, J., Norton, K. P., Hall, A., & Hattestrand, C. (2012). Meteoric <sup>10</sup>Be concentrations from saprolite and till in northern Sweden: Implications for glacial erosion and age. *Quaternary Geochronology*, 12, 11–22. <https://doi.org/10.1016/j.quageo.2012.05.005>
- Ehlers, J., & Gibbard, P. L. (2004). *Quaternary glaciations: Extent and chronology*. Elsevier.
- Erlanger, E. D., Rugenstein, J. K. C., Bufe, A., Picotti, V., & Willett, S. D. (2021). Controls on physical and chemical denudation in a mixed carbonate-siliciclastic orogen. *Journal of Geophysical Research: Earth Surface*, 126(8), e2021JF006064. <https://doi.org/10.1029/2021jf006064>
- Ford, D., & Williams, P. (2007). *Karst hydrogeology and geomorphology*. Wiley.
- Frank, M., Porcelli, D., Andersson, P., Baskaran, M., Bjork, G., Kubik, P. W., et al. (2009). The dissolved Beryllium isotope composition of the Arctic Ocean. *Geochimica et Cosmochimica Acta*, 73(20), 6114–6133. <https://doi.org/10.1016/j.gca.2009.07.010>
- Gabrovšek, F. (2009). On concepts and methods for the estimation of dissolutional denudation rates in karst areas. *Geomorphology*, 106(1–2), 9–14. <https://doi.org/10.1016/j.geomorph.2008.09.008>
- Gaillardet, J., Calmels, D., Romero-Mujalli, G., Zakharova, E., & Hartmann, J. (2018). Global climate control on carbonate weathering intensity. *Chemical Geology*, 527, 118762. <https://doi.org/10.1016/j.chemgeo.2018.05.009>
- Gaillardet, J., Dupré, B., Louvat, P., & Allègre, C. J. (1999). Global silicate weathering and CO<sub>2</sub> consumption rates deduced from the chemistry of large rivers. *Chemical Geology*, 159(1–4), 3–30. [https://doi.org/10.1016/s0009-2541\(99\)00031-5](https://doi.org/10.1016/s0009-2541(99)00031-5)
- Gao, S., Luo, T. C., Zhang, B. R., Zhang, H. F., Han, Y. W., Zhao, Z. D., & Hu, Y. K. (1998). Chemical composition of the continental crust as revealed by studies in East China. *Geochimica et Cosmochimica Acta*, 62(11), 1959–1975. [https://doi.org/10.1016/S0016-7037\(98\)00121-5](https://doi.org/10.1016/S0016-7037(98)00121-5)
- Godard, V., Ollivier, V., Bellier, O., Miramont, C., Shabanian, E., Fleury, J., et al. (2016). Weathering-limited hillslope evolution in carbonate landscapes. *Earth and Planetary Science Letters*, 446, 10–20. <https://doi.org/10.1016/j.epsl.2016.04.017>
- Goldscheider, N., Chen, Z., Auler, A. S., Bakalowicz, M., Broda, S., Drew, D., et al. (2020). Global distribution of carbonate rocks and karst water resources. *Hydrogeology Journal*, 28(5), 1661–1677. <https://doi.org/10.1007/s10040-020-02139-5>
- Goudie, A. S., & Middleton, N. J. (2001). Saharan dust storms: Nature and consequences. *Earth-Science Reviews*, 56(1–4), 179–204. [https://doi.org/10.1016/S0012-8252\(01\)00067-8](https://doi.org/10.1016/S0012-8252(01)00067-8)
- Graly, J. A., Reusser, L. J., & Bierman, P. R. (2011). Short and long-term delivery rates of meteoric <sup>10</sup>Be to terrestrial soils. *Earth and Planetary Science Letters*, 302(3–4), 329–336. <https://doi.org/10.1016/j.epsl.2010.12.020>
- Granger, D. E., & Schaller, M. (2014). Cosmogenic nuclides and erosion at the watershed scale. *Elements*, 10(5), 369–373. <https://doi.org/10.2113/gselements.10.5.369>
- Grew, E. S. (2002). Mineralogy, petrology and geochemistry of beryllium: An introduction and list of beryllium minerals. *Reviews in Mineralogy and Geochemistry*, 50(1), 1–76. <https://doi.org/10.2138/rmg.2202.50.01>
- Gunn, J. (1981). Limestone solution rates and processes in the Waitomo District, New Zealand. *Earth Surface Processes and Landforms*, 6(5), 427–445. <https://doi.org/10.1002/esp.3290060504>
- Gunn, J. (2013). 6.7 denudation and erosion rates in karst. In *Treatise on geomorphology* (pp. 72–81). <https://doi.org/10.1016/b978-0-12-374739-6.00115-9>
- Han, G., & Liu, C.-Q. (2004). Water geochemistry controlled by carbonate dissolution: A study of the river waters draining karst-dominated terrain, Guizhou Province, China. *Chemical Geology*, 204(1–2), 1–21. <https://doi.org/10.1016/j.chemgeo.2003.09.009>
- Hartmann, A., Goldscheider, N., Wagener, T., Lange, J., & Weiler, M. (2014). Karst water resources in a changing world: Review of hydrological modeling approaches. *Reviews of Geophysics*, 52(3), 218–242. <https://doi.org/10.1002/2013rg000443>

- Hartmann, J., Lauerwald, R., & Moosdorf, N. (2014). A brief overview of the GLObal River chemistry database, GLORICH. *Procedia Earth and Planetary Science*, 10, 23–27. <https://doi.org/10.1016/j.proeps.2014.08.005>
- Hartmann, J., & Moosdorf, N. (2011). Coupling spatial geochemical and lithological information to distinguish silicate and non-silicate chemical weathering fluxes. *Applied Geochemistry*, 26, S281–S284. <https://doi.org/10.1016/j.apgeochem.2011.03.081>
- Hartmann, J., & Moosdorf, N. (2012). The new global lithological map database GLIM: A representation of rock properties at the Earth surface. *Geochemistry, Geophysics, Geosystems*, 13(12), Q12004. <https://doi.org/10.1029/2012gc004370>
- Heikkilä, U., Muscheler, R., & Smith, A. M. (2013). Phase of solar activity affects response of solar proxy  $^{10}\text{Be}$ . *Earth and Planetary Science Letters*, 380, 72–76. <https://doi.org/10.1016/j.epsl.2013.08.036>
- Heikkilä, U., Shi, X., Phipps, S. J., & Smith, A. M. (2014).  $^{10}\text{Be}$  in late deglacial climate simulated by ECHAM5-HAM—Part 2: Isolating the solar signal from  $^{10}\text{Be}$  deposition. *Climate of the Past*, 10(2), 687–696. <https://doi.org/10.5194/cp-10-687-2014>
- Heikkilä, U., & von Blanckenburg, F. (2015). The global distribution of Holocene meteoric  $^{10}\text{Be}$  fluxes from atmospheric models. Distribution maps for terrestrial Earth surface applications. *GFZ Data Services*. <https://doi.org/10.5880/GFZ.3.4.2015.001>
- Hohl, S. V., Becker, H., Herzlieb, S., & Guo, Q. (2015). Multiproxy constraints on alteration and primary compositions of Ediacaran deep-water carbonate rocks, Yangtze Platform, South China. *Geochimica et Cosmochimica Acta*, 163, 262–278. <https://doi.org/10.1016/j.gca.2015.04.037>
- Jacobson, A. D., Blum, J. D., Chamberlain, C. P., Poage, M. A., & Sloan, V. F. (2002). Ca/Sr and Sr isotope systematics of a Himalayan glacial chronosequence: Carbonate versus silicate weathering rates as a function of landscape surface age. *Geochimica et Cosmochimica Acta*, 66(1), 13–27. [https://doi.org/10.1016/S0016-7037\(01\)00755-4](https://doi.org/10.1016/S0016-7037(01)00755-4)
- Jeandel, C. (1993). Concentration and isotopic composition of Nd in the South Atlantic Ocean. *Earth and Planetary Science Letters*, 117(3–4), 581–591. [https://doi.org/10.1016/0012-821X\(93\)90104-H](https://doi.org/10.1016/0012-821X(93)90104-H)
- Jeannin, P.-Y., Hessenauer, M., Malard, A., & Chapuis, V. (2016). Impact of global change on karst groundwater mineralization in the Jura Mountains. *Science of the Total Environment*, 541, 1208–1221. <https://doi.org/10.1016/j.scitotenv.2015.10.008>
- Kaufmann, G., & Braun, J. (2000). Karst Aquifer evolution in fractured, porous rocks. *Water Resources Research*, 36(6), 1381–1391. <https://doi.org/10.1029/1999WR900356>
- Kessler, J., & Chambraud, A. (1986). La météo de la France, Tous les climats par localité.
- Kirchner, J. W., Finkel, R. C., Riebe, C. S., Granger, D. E., Clayton, J. L., King, J. G., & Megahan, W. F. (2001). Mountain erosion over 10 yr, 10 k.y., and 10 m.y. time scales. *Geology*, 29(7), 591–594. <https://doi.org/10.1130/0091-7613>
- Klein, M. G., Gottgang, A., Mous, D. J. W., Bourlès, D. L., Arnold, M., Hamelin, B., et al. (2008). Performance of the HVE 5MV AMS system at CEREGE using an absorber foil for isobar suppression. *Nuclear Instruments and Methods in Physics Research Section B: Beam Interactions with Materials and Atoms*, 266(8), 1828–1832. <https://doi.org/10.1016/j.nimb.2007.11.077>
- Lal, D. (1991). Cosmic ray labeling of erosion surfaces: In situ nuclide production rates and erosion models. *Earth and Planetary Science Letters*, 104(2–4), 424–439. [https://doi.org/10.1016/0012-821X\(91\)90220-c](https://doi.org/10.1016/0012-821X(91)90220-c)
- Le Roux, G., Fagel, N., De Vleeschouwer, F., Krachler, M., Debaille, V., Stille, P., et al. (2012). Volcano- and climate-driven changes in atmospheric dust sources and fluxes since the Late Glacial in Central Europe. *Geology*, 40(4), 335–338. <https://doi.org/10.1130/g32586.1>
- Liu, Y., Wagener, T., Beck, H. E., & Hartmann, A. (2020). What is the hydrologically effective area of a catchment? *Environmental Research Letters*, 15(10), 104024. <https://doi.org/10.1088/1748-9326/aba7e5>
- Magny, M. (1992). Holocene lake-level fluctuations in Jura and the northern subalpine ranges, France: Regional pattern and climatic implications. *Boreas*, 21(4), 319–334. <https://doi.org/10.1111/j.1502-3885.1992.tb00038.x>
- Magny, M., Peyron, O., Gauthier, E., Vannièrè, B., Millet, L., & Vermot-Desroches, B. (2017). Quantitative estimates of temperature and precipitation changes over the last millennium from pollen and lake-level data at Lake Joux, Swiss Jura Mountains. *Quaternary Research*, 75(1), 45–54. <https://doi.org/10.1016/j.yqres.2010.11.001>
- Mathey, M., Doin, M. P., André, P., Walpersdorf, A., Baize, S., & Sue, C. (2022). Spatial heterogeneity of uplift pattern in the western European Alps revealed by InSAR time-series analysis. *Geophysical Research Letters*, 49(1), e2021GL095744. <https://doi.org/10.1029/2021gl095744>
- Matsushi, Y., Sasa, K., Takahashi, T., Sueki, K., Nagashima, Y., & Matsukura, Y. (2010). Denudation rates of carbonate pinnacles in Japanese karst areas: Estimates from cosmogenic  $^{36}\text{Cl}$  in calcite. *Nuclear Instruments and Methods in Physics Research Section B: Beam Interactions with Materials and Atoms*, 268(7–8), 1205–1208. <https://doi.org/10.1016/j.nimb.2009.10.134>
- Nevers, P., Bouchez, J., Gaillardet, J., Thomazo, C., Charpentier, D., Faure, L., & Bertrand, C. (2021). Landslides as geological hotspots of  $\text{CO}_2$  emission: Clues from the instrumented Séchilienne landslide, western European Alps. *Earth Surface Dynamics*, 9(3), 487–504. <https://doi.org/10.5194/esurf-9-487-2021>
- Ott, R. F., Gallen, S. F., Caves Rugenstein, J. K., Ivy-Ochs, S., Helman, D., Fassoulas, C., et al. (2019). Chemical versus mechanical denudation in meta-clastic and carbonate bedrock catchments on Crete, Greece, and mechanisms for steep and high carbonate topography. *Journal of Geophysical Research: Earth Surface*, 124(12), 2943–2961. <https://doi.org/10.1029/2019jf005142>
- Ott, R. F., Gallen, S. F., & Granger, D. E. (2022). Cosmogenic nuclide weathering biases: Corrections and potential for denudation and weathering rate measurements. *Geochronology Discuss*, 2022, 1–25. <https://doi.org/10.5194/gchron-2022-5>
- Portenga, E. W., Bierman, P. R., Trodick, C. D., Greene, S. E., DeJong, B. D., Rood, D. H., & Pavich, M. J. (2019). Erosion rates and sediment flux within the Potomac River basin quantified over millennial timescales using beryllium isotopes. *GSA Bulletin*, 131(7–8), 1295–1311. <https://doi.org/10.1130/b31840.1>
- Rahaman, W., Wittmann, H., & von Blanckenburg, F. (2017). Denudation rates and the degree of chemical weathering in the Ganga basin from ratios of meteoric cosmogenic  $^{10}\text{Be}$  to stable  $^9\text{Be}$ . *Earth and Planetary Science Letters*, 469, 156–169. <https://doi.org/10.1016/j.epsl.2017.04.001>
- Repasch, M., Wittmann, H., Scheingross, J. S., Sachse, D., Szupiany, R., Orfeo, O., et al. (2020). Sediment transit time and floodplain storage dynamics in alluvial rivers revealed by meteoric  $^{10}\text{Be}$ . *Journal of Geophysical Research: Earth Surface*, 125(7), e2019JF005419. <https://doi.org/10.1029/2019jf005419>
- Riebe, C. S., Kirchner, J. W., & Finkel, R. C. (2003). Long-term rates of chemical weathering and physical erosion from cosmogenic nuclides and geochemical mass balance. *Geochimica et Cosmochimica Acta*, 67(22), 4411–4427. [https://doi.org/10.1016/s0016-7037\(03\)00382-x](https://doi.org/10.1016/s0016-7037(03)00382-x)
- Romero-Mujallí, G., Hartmann, J., Börker, J., Gaillardet, J., & Calmels, D. (2019). Ecosystem controlled soil-rock  $\text{pCO}_2$  and carbonate weathering—Constraints by temperature and soil water content. *Chemical Geology*, 527, 118634. <https://doi.org/10.1016/j.chemgeo.2018.01.030>
- Rudnick, R. L., & Gao, S. (2004). Composition of the continental crust. In D. H. Heinrich, & K. T. Karl (Eds.), *Treatise on geochemistry* (pp. 1–64). Elsevier.
- Ryb, U., Matmon, A., Erel, Y., Haviv, I., Benedetti, L., & Hidy, A. J. (2014a). Styles and rates of long-term denudation in carbonate terrains under a Mediterranean to hyper-arid climatic gradient. *Earth and Planetary Science Letters*, 406, 142–152. <https://doi.org/10.1016/j.epsl.2014.09.008>
- Ryb, U., Matmon, A., Erel, Y., Haviv, I., Katz, A., Starinsky, A., et al. (2014b). Controls on denudation rates in tectonically stable Mediterranean carbonate terrain. *Geological Society of America Bulletin*, 126(3–4), 553–568. <https://doi.org/10.1130/b30886.1>

- Sadier, B., Delannoy, J. J., Benedetti, L., Bourles, D. L., Jaillet, S., Geneste, J. M., et al. (2012). Further constraints on the Chauvet cave artwork elaboration. *Proceedings of the National Academy of Sciences of the United States of America*, 109(21), 8002–8006. <https://doi.org/10.1073/pnas.1118593109>
- Schlatter, A., Schneider, D., Geiger, A., & Kahle, H.-G. (2005). Recent vertical movements from precise levelling in the vicinity of the city of Basel, Switzerland. *International Journal of Earth Sciences*, 94(4), 507–514. <https://doi.org/10.1007/s00531-004-0449-9>
- Schmidbaur, H. (2001). Recent contributions to the aqueous coordination chemistry of beryllium. *Coordination Chemistry Reviews*, 215(1), 223–242. [https://doi.org/10.1016/S0010-8545\(00\)00406-9](https://doi.org/10.1016/S0010-8545(00)00406-9)
- Shen, C., Beer, J., Kubik, P. W., Suter, M., Borkovec, M., & Liu, T. S. (2004). Grain size distribution,  $^{10}\text{Be}$  content and magnetic susceptibility of micrometer-nanometer loess materials. *Nuclear Instruments and Methods in Physics Research Section B: Beam Interactions with Materials and Atoms*, 223–224, 613–617. <https://doi.org/10.1016/j.nimb.2004.04.113>
- Shen, C. D., Beer, J., Kubik, P. W., Sun, W. D., Liu, T. S., & Liu, K. X. (2010).  $^{10}\text{Be}$  in desert sands, falling dust and loess in China. *Nuclear Instruments and Methods in Physics Research Section B: Beam Interactions with Materials and Atoms*, 268(7–8), 1050–1053. <https://doi.org/10.1016/j.nimb.2009.10.095>
- Singleton, A. A., Schmidt, A. H., Bierman, P. R., Rood, D. H., Neilson, T. B., Greene, E. S., et al. (2017). Effects of grain size, mineralogy, and acid-extractable grain coatings on the distribution of the fallout radionuclides  $^7\text{Be}$ ,  $^{10}\text{Be}$ ,  $^{137}\text{Cs}$ , and  $^{210}\text{Pb}$  in river sediment. *Geochimica et Cosmochimica Acta*, 197, 71–86. <https://doi.org/10.1016/j.gca.2016.10.007>
- Stallard, R. F., & Edmond, J. M. (1987). Geochemistry of the Amazon: 3. Weathering chemistry and limits to dissolved inputs. *Journal of Geophysical Research*, 92(C8), 8293–8302. <https://doi.org/10.1029/JC092iC08p08293>
- Staudigel, H., Albarède, F., Blichert-Toft, J., Edmond, J., McDonough, B., Jacobsen, S. B., et al. (1998). Geochemical Earth reference model (GERM): Description of the initiative. *Chemical Geology*, 145(3–4), 153–159. [https://doi.org/10.1016/S0009-2541\(97\)00141-1](https://doi.org/10.1016/S0009-2541(97)00141-1)
- Stets, E. G., Butman, D., McDonald, C. P., Stackpoole, S. M., DeGrandpre, M. D., & Striegl, R. G. (2017). Carbonate buffering and metabolic controls on carbon dioxide in rivers. *Global Biogeochemical Cycles*, 31(4), 663–677. <https://doi.org/10.1002/2016gb005578>
- Stone, J., Allan, G. L., Fifield, L. K., Evans, J. M., & Chivas, A. R. (1994). Limestone erosion measurements with cosmogenic chlorine-36 in calcite—Preliminary results from Australia. *Nuclear Instruments and Methods in Physics Research Section B: Beam Interactions with Materials and Atoms*, 92(1), 311–316. [https://doi.org/10.1016/0168-583X\(94\)96025-9](https://doi.org/10.1016/0168-583X(94)96025-9)
- Stone, J. O., Allan, G. L., Fifield, L. K., & Cresswell, R. G. (1996). Cosmogenic chlorine-36 from calcium spallation. *Geochimica et Cosmochimica Acta*, 60(4), 679–692. [https://doi.org/10.1016/0016-7037\(95\)00429-7](https://doi.org/10.1016/0016-7037(95)00429-7)
- Tavant, Y., Tavant, H., & Bruckert, S. (1994). Variation du carbone organique en fonction des propriétés des sols et de l'altitude dans le Jura (France). *Geoderma*, 61(1–2), 133–141. [https://doi.org/10.1016/0016-7061\(94\)90015-9](https://doi.org/10.1016/0016-7061(94)90015-9)
- Taylor, A., Blake, W. H., Couldrick, L., & Keith-Roach, M. J. (2012). Sorption behaviour of Beryllium-7 and implications for its use as a sediment tracer. *Geoderma*, 187–188, 16–23. <https://doi.org/10.1016/j.geoderma.2012.04.013>
- Thomas, F., Godard, V., Bellier, O., Benedetti, L., Ollivier, V., Rizza, M., et al. (2018). Limited influence of climatic gradients on the denudation of a Mediterranean carbonate landscape. *Geomorphology*, 316, 44–58. <https://doi.org/10.1016/j.geomorph.2018.04.014>
- Thomas, F., Godard, V., Bellier, O., Shabanian, E., Ollivier, V., Benedetti, L., et al. (2017). Morphological controls on the dynamics of carbonate landscapes under a Mediterranean climate. *Terra Nova*, 29(3), 173–182. <https://doi.org/10.1111/ter.12260>
- von Blanckenburg, F. (2005). The control mechanisms of erosion and weathering at basin scale from cosmogenic nuclides in river sediment. *Earth and Planetary Science Letters*, 237(3–4), 462–479. <https://doi.org/10.1016/j.epsl.2005.06.030>
- von Blanckenburg, F., Belshaw, N. S., & O'Nions, R. K. (1996). Separation of  $^9\text{Be}$  and cosmogenic  $^{10}\text{Be}$  from environmental materials and SIMS isotope dilution analysis. *Chemical Geology*, 129(1–2), 93–99. [https://doi.org/10.1016/0009-2541\(95\)00157-3](https://doi.org/10.1016/0009-2541(95)00157-3)
- von Blanckenburg, F., & Bouchez, J. (2014). River fluxes to the sea from the ocean's  $^{10}\text{Be}/^9\text{Be}$  ratio. *Earth and Planetary Science Letters*, 387(0), 34–43. <https://doi.org/10.1016/j.epsl.2013.11.004>
- von Blanckenburg, F., Bouchez, J., & Wittmann, H. (2012). Earth surface erosion and weathering from the  $^{10}\text{Be}$  (meteoric)/ $^9\text{Be}$  ratio. *Earth and Planetary Science Letters*, 351–352, 295–305. <https://doi.org/10.1016/j.epsl.2012.07.022>
- White, W. B. (1988). *Geomorphology and hydrology of karst terrains*. Oxford University Press.
- Willenbring, J. K., & von Blanckenburg, F. (2010). Meteoric cosmogenic Beryllium-10 adsorbed to river sediment and soil: Applications for Earth-surface dynamics. *Earth-Science Reviews*, 98(1–2), 105–122. <https://doi.org/10.1016/j.earscirev.2009.10.008>
- Wittmann, H., Bouchez, J., Calmels, D., Gaillardet, J., Frick, D., Stronck, N., et al. (2024). Denudation and weathering rates of carbonate landscapes from meteoric  $^{10}\text{Be}/^9\text{Be}$  ratios [Dataset]. *GFZ German Research Centre for Geosciences*. <https://doi.org/10.5880/GFZ.3.3.2024.001>
- Wittmann, H., & von Blanckenburg, F. (2016). The geological significance of cosmogenic nuclides in large lowland river basins. *Earth-Science Reviews*, 159, 118–141. <https://doi.org/10.1016/j.earscirev.2016.06.001>
- Wittmann, H., von Blanckenburg, F., Bouchez, J., Dannhaus, N., Naumann, R., Christl, M., & Gaillardet, J. (2012). The dependence of meteoric  $^{10}\text{Be}$  concentrations on particle size in Amazon River bed sediment and the extraction of reactive  $^{10}\text{Be}/^9\text{Be}$  ratios. *Chemical Geology*, 318–319, 126–138. <https://doi.org/10.1016/j.chemgeo.2012.04.031>
- Wittmann, H., von Blanckenburg, F., Dannhaus, N., Bouchez, J., Gaillardet, J., Guyot, J. L., et al. (2015). A test of the cosmogenic  $^{10}\text{Be}$  (meteoric)/ $^9\text{Be}$  proxy for simultaneously determining basin-wide erosion rates, denudation rates, and the degree of weathering in the Amazon basin. *Journal of Geophysical Research: Earth Surface*, 120(12), 2498–2528. <https://doi.org/10.1002/2015jf003581>
- Xiao, H., & Weng, Q. (2007). The impact of land use and land cover changes on land surface temperature in a karst area of China. *Journal of Environmental Management*, 85(1), 245–257. <https://doi.org/10.1016/j.jenvman.2006.07.016>
- Xu, S., Liu, C., Freeman, S., Lang, Y., Schnabel, C., Tu, C., et al. (2013). In-situ cosmogenic  $^{36}\text{Cl}$  denudation rates of carbonates in Guizhou karst area. *Chinese Science Bulletin*, 58(20), 2473–2479. <https://doi.org/10.1007/s11434-013-5756-8>
- Yang, Y., Lang, Y.-C., Xu, S., Liu, C.-Q., Cui, L.-F., Freeman, S. P. H. T., & Wilken, K. M. (2020). Combined unsteady denudation and climatic gradient factors constrain carbonate landscape evolution: New insights from in situ cosmogenic  $^{36}\text{Cl}$ . *Quaternary Geochronology*, 58, 101075. <https://doi.org/10.1016/j.quageo.2020.101075>
- Yang, Y., Zhang, S.-C., Zhang, J.-X., Cui, L.-F., Liu, C.-Q., & Xu, S. (2024). Quantifying denudation rates and sediment recycling of low-relief, high-elevation landscapes using in-situ and meteoric cosmogenic nuclides. *Geochimica et Cosmochimica Acta*, 370, 78–88. <https://doi.org/10.1016/j.gca.2024.02.014>
- You, C.-F., Lee, T., & Li, Y.-H. (1989). The partition of Be between soil and water. *Chemical Geology*, 77(2), 105–118. [https://doi.org/10.1016/0009-2541\(89\)90136-8](https://doi.org/10.1016/0009-2541(89)90136-8)